Article

Single-cell dissection of the human brain vasculature

https://doi.org/10.1038/s41586-022-04521-7

Received: 6 April 2021

Accepted: 4 February 2022

Published online: 14 February 2022

Check for updates

Francisco J. Garcia[1,2,3,10], Na Sun[3,4,5,10], Hyeseung Lee[2,3], Brianna Godlewski[6,7], Hansruedi Mathys[2,3,8], Kyriaki Galani[3,4,5], Blake Zhou[2,3], Xueqiao Jiang[2,3], Ayesha P. Ng[2,3], Julio Mantero[3,4,5], Li-Huei Tsai[1,2,3], David A. Bennett[9], Mustafa Sahin[6,7], Manolis Kellis[3,4,5]✉ & Myriam Heiman[1,2,3]✉

Despite the importance of the cerebrovasculature in maintaining normal brain physiology and in understanding neurodegeneration and drug delivery to the central nervous system[1], human cerebrovascular cells remain poorly characterized owing to their sparsity and dispersion. Here we perform single-cell characterization of the human cerebrovasculature using both ex vivo fresh tissue experimental enrichment and post mortem in silico sorting of human cortical tissue samples. We capture 16,681 cerebrovascular nuclei across 11 subtypes, including endothelial cells, mural cells and three distinct subtypes of perivascular fibroblast along the vasculature. We uncover human-specific expression patterns along the arteriovenous axis and determine previously uncharacterized cell-type-specific markers. We use these human-specific signatures to study changes in 3,945 cerebrovascular cells from patients with Huntington's disease, which reveal activation of innate immune signalling in vascular and glial cell types and a concomitant reduction in the levels of proteins critical for maintenance of blood–brain barrier integrity. Finally, our study provides a comprehensive molecular atlas of the human cerebrovasculature to guide future biological and therapeutic studies.

The cerebrovasculature exhibits specialized barrier properties that regulate the transport of biomolecules and maintain brain homeostasis. Structural imaging and molecular studies have yielded important insights into the mouse cerebrovasculature[2–4]. However, human brains exhibit increased complexity and energetic needs, probably accompanied by human-specific adaptations, which remain uncharacterized. Moreover, cerebrovascular dysfunction and blood–brain barrier (BBB) breakdown are thought to have important roles not only in ageing[5] but also in neurodegenerative diseases[6]. Thus, understanding the human cerebrovasculature, both in physiologic and pathological conditions, is a pressing need for scientific and clinical reasons.

Here we address this challenge by reporting a comprehensive single-cell molecular atlas of human cerebrovasculature cells, across ≈17,000 nuclei from ex vivo freshly resected surgical human brain tissue using a cerebrovascular cell enrichment protocol, and an in silico cell sorting from post mortem human brain tissue. We computationally integrate these datasets to characterize 11 subtypes of cells, including endothelial, mural and perivascular fibroblast cell subtypes. Our studies reveal human-specific transcriptomic signatures along the arteriovenous axis and elucidate transcriptional changes in cerebrovasculature cell types in Huntington's disease (HD). Our study highlights the unique cell-type-specific and species-specific characteristics in humans and provides a framework for mechanistic dissection of pathological state dysfunctions.

Ex vivo and in silico vasculature enrichment

Owing to low abundance in the brain and poor capture efficiency with droplet-based sequencing methodologies, cerebrovasculature cells have been challenging to characterize at single-cell resolution. Previous studies in mice have used transgenic reporter lines and fluorescence-activated cell sorting to enrich for cerebrovasculature cells[4], but these methods are incompatible with human studies. To address this challenge, we developed a blood vessel enrichment (BVE) protocol (Fig. 1a, top) to enrich for human vascular cell types from fresh and frozen brain tissue for single-cell applications by dextran-based density ultracentrifugation[7], and used the resulting microvessel-enriched pellet as input for single-nucleus RNA-seq (snRNA-seq) profiling[8]. We validated our protocol using mouse cortical samples, showing enrichment for markers of endothelial and mural cells (Extended Data Fig. 1a), and no enrichment for other cell types. However, we found that our purification captured astrocytic endfeet[7], as they remain attached to the vasculature post-enrichment (Extended Data Fig. 1b).

[1]Department of Brain and Cognitive Sciences, MIT, Cambridge, MA, USA. [2]Picower Institute for Learning and Memory, Cambridge, MA, USA. [3]Broad Institute of MIT and Harvard, Cambridge, MA, USA. [4]Department of Electrical Engineering and Computer Science, MIT, Cambridge, MA, USA. [5]MIT Computer Science and Artificial Intelligence Laboratory, Cambridge, MA, USA. [6]Rosamund Stone Zander Translational Neuroscience Center, F.M. Kirby Neurobiology Center, Department of Neurology, Boston Children's Hospital, Boston, MA, USA. [7]Department of Neurology, Harvard Medical School, Boston, MA, USA. [8]Department of Neurobiology, University of Pittsburgh School of Medicine, Pittsburgh, PA, USA. [9]Rush Alzheimer's Disease Center, Rush University Medical Center, Chicago, IL, USA. [10]These authors contributed equally: Francisco J. Garcia, Na Sun. ✉e-mail: manoli@mit.edu; mheiman@mit.edu

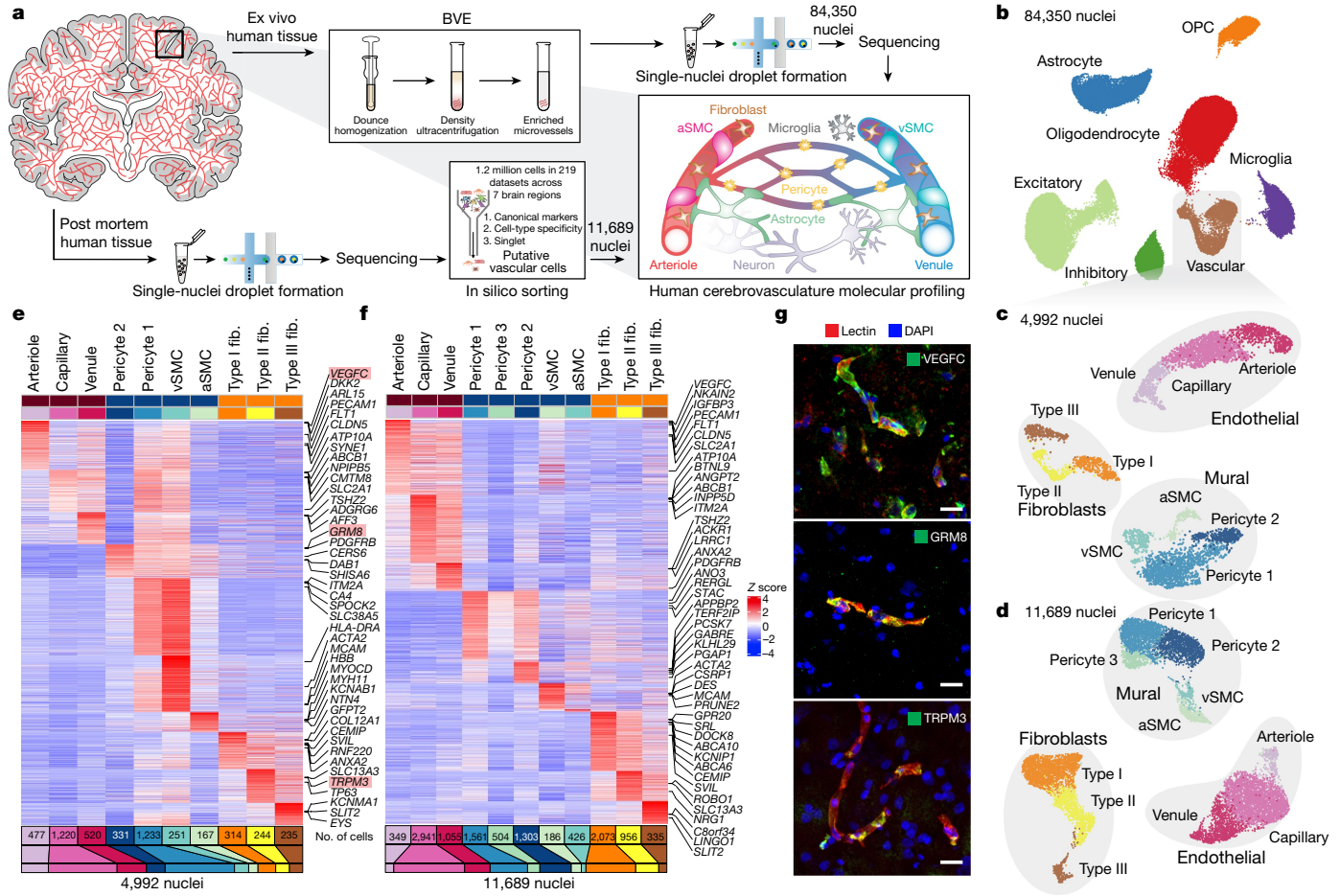

Fig. 1 | snRNA-seq profiling of the human cerebrovasculature. **a**, Experimental schematic. **b**, Global uniform manifold approximation and projection (UMAP) of 84,350 profiled nuclei from ex vivo human temporal cortex. OPC, oligodendrocyte precursor cell. **c**, UMAP of 4,992 profiled vascular nuclei from the cluster highlighted in **b**. **d**, UMAP of 11,689 in silico-sorted vascular nuclei from post mortem human brains. **e**, **f**, Genes expressed at high levels in the subclusters in **c** and **d**, respectively. Fib., fibroblast. **g**, Validation of expression of the markers VEGFC, GRM8 and TRPM3 (highlighted in pink in **e**) by indirect immunofluorescence staining (each in green pseudocolour). Representative images shown from $n = 3$ independent biological replicates for each marker. Brightness and contrast enhanced for visualization. DAPI, 4′,6-diamidino-2-phenylindole. Scale bars, 20 µm.

We applied our BVE protocol to ex vivo fresh-frozen tissue from 17 temporal lobe surgical resections of patients with intractable epilepsy, selecting only healthy tissue distal to epileptic foci (Supplementary Table 1), thus providing samples free from hypoxia and death-induced effects, and avoiding the decreased RNA quality associated with long post mortem intervals. For seven samples, we used standard snRNA-seq[9] to confirm the absence of BVE-induced biases (Extended Data Fig. 2a, b). We next complemented our BVE-captured dataset with in silico sorting of data from post mortem samples across seven different brain regions from control individuals without neurological pathology as part of the Religious Orders Study and Rush Memory and Aging Project (ROSMAP) cohort[10] and reported here. We used a combination of canonical vasculature markers and whole-transcriptome cellular signatures, separately from our BVE protocol, to ensure independence (Fig. 1a, bottom, Methods).

After quality control, from the ex vivo samples, we obtained 84,350 single nuclei (Fig. 1b and Extended Data Fig. 2c–e), including 16 subtypes of excitatory neurons, 6 subtypes of inhibitory neurons, oligodendrocytes, oligodendrocyte precursor cells, astrocytes and microglia. From the ex vivo samples, we also profiled 4,992 vascular cells, a 13.7-fold enrichment from previous studies[8] (5.48% versus ≈0.4%), and complemented this with 11,689 cells sorted in silico. We distinguished 11 subtypes of vascular cells (Fig. 1c, d), including (ex vivo/in silico): 3 subtypes of endothelial cells ($n = 2,217/4,345$); 5 subtypes of mural cells ($n = 1,982/3,980$), including 1,564/3,358 pericytes and 418/622 smooth muscle cells (SMCs); and 3 subtypes of perivascular fibroblasts ($n = 793/3,364$). Most cerebrovascular subtypes in the ex vivo BVE dataset were also found in our post mortem in silico-sorted dataset, validating the consistency of cell types across experimental platforms and sample cohorts. Pericytes exhibited greater heterogeneity in the in silico-sorted dataset (3 versus 2 subtypes), although this may be due to a larger number of profiled cells compared to the ex vivo dataset.

Genes and pathways defining cell types

We next created an atlas of human cerebrovascular cells and revealed their defining molecular characteristics by combining our experimental and computational enrichment strategies. We found robust expression of 17,212 genes (each in 50+ cells), including 3,164 differentially expressed genes among cell types (ctDEGs) in ex vivo and 3,470 ctDEGs in post mortem datasets, which expanded the previously known set of canonical markers for each cell type and enabled us to infer candidate functional roles for each cell type. We confirmed robust differential expression for known marker genes in endothelial (*CLDN5*), mural (*TAGLN*), fibroblast (*CEMIP*), astroglial (*GFAP*), neuronal (*CAMK2A*), oligodendrocyte (*PLP1*) and microglial (*CSF1R*) cell types (Fig. 1e, f and Supplementary Table 2). In addition, we identified markers for subtypes of these cells, separating endothelial cells into arteriole (*VEGFC*

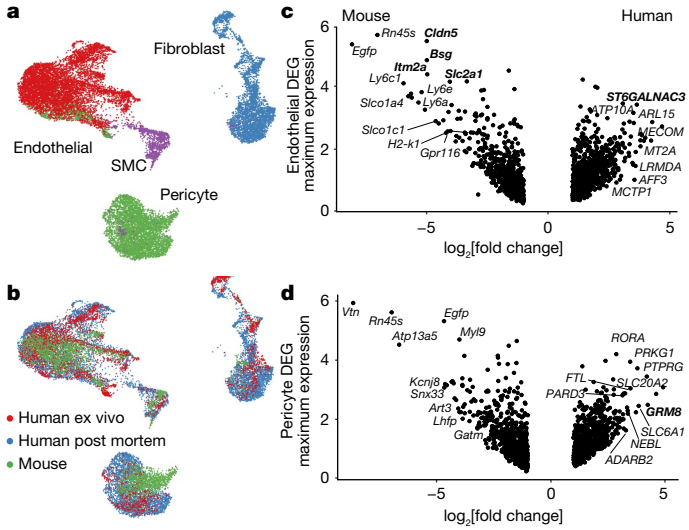

Fig. 2 | Integrative analysis of human ex vivo, post mortem and mouse cerebrovascular cell types. a, **b**, UMAP visualization of integrated cells from human ex vivo, human post mortem and mouse, coloured by cell types (**a**) and data source (**b**). **c**, **d**, hmDEGs in endothelial cells (**c**) and pericytes (**d**). The *x* axis represents the log-transformed fold change and the *y* axis represents the maximal expression level. The top genes are highlighted for mouse (left) and human (right). Genes that were also cell-type markers are shown in bold.

and *ARL15*), capillary (*MFSD2A* and *SLC7A5*) and venule (*TSHZ2* and *ADGRG6*), mural cells into arteriolar SMC (aSMC) (*ACTA2* and *MYH11*), venular SMC (vSMC) (*MYOCD* and *CD74*) and pericytes (*GRM8* and *PDGFRB*), and fibroblasts into type I (*ABCA10* and *FBLN1*), type II (*TRPM3* and *MYRIP*) and type III (*KCNMA1* and *SLC4A4*).

Several of these marker genes, including *ARL15*, *TSHZ2*, *GRM8* and *TRPM3*, have not previously been identified for cerebrovascular cell types. We confirmed that these ctDEGs and corresponding cell types were consistent between our ex vivo and post mortem samples (Extended Data Fig. 2f), indicating that they hold across sample types and methodologies. Indeed, the marker genes *VEGFC*, *GRM8* and *TRPM3* exhibited corresponding protein expression in human cerebrovascular cell types by immunofluorescence (Fig. 1g).

Integration of human and mouse snRNA-seq

To evaluate whether cerebrovasculature expression profiles are conserved across species and platforms, we used canonical correlation analysis to integrate 4,992 ex vivo and 11,689 post mortem human cells with 3,406 C57BL/6 mouse cells[4]. To match cell types and correct for species and experimental differences, we projected each cell on a common two-dimensional embedding that corrects for covariates (age, sex, regions, sequencing platforms and post-mortem interval) (Extended Data Fig. 3a, b), and found broad cell-type conservation across species and platforms (Fig. 2a, b and Extended Data Fig. 3c, d).

Despite sharing cell-type identities, we found extensive expression differences between species, with 7.3% of genes showing on average twofold changes ($n = 1{,}261$) for each cell type, and 15.6% of these human–mouse DEGs (hmDEGs) being uniquely expressed in one species (Extended Data Fig. 3e and Supplementary Table 3). Whereas endothelial cells and SMCs showed no significant differences in cell-type proportions, pericytes and type II fibroblasts showed differential proportions (Extended Data Fig. 3f). These observed differences in expression did not stem from proportion changes, as they were not enriched for cell-type marker genes (Extended Data Fig. 3g). hmDEGs were highly consistent between ex vivo and post mortem samples (80% agreement, $P < 2.2 \times 10^{-16}$). In each cell type, hmDEGs were strongly enriched for ctDEGs (12× endothelial cells, 14× fibroblasts, 15× pericytes, 9× SMCs), indicating that cell-type identity markers vary highly between species.

hmDEGs showed cell-type-specific gene ontology enrichments that provide insight into species-specific functional specialization. For example, endothelial cells showed 742 human-increased genes, with enrichments in regulation of axonogenesis (Fig. 2c and Extended Data Fig. 3h), whereas pericytes showed 650 human-increased genes enriched in regulation of endothelial cell migration (Fig. 2d and Extended Data Fig. 3i). Similarly, SMCs showed 469 human-increased and 641 mouse-increased genes (Extended Data Fig. 3j), respectively, whereas fibroblasts showed 308 human-increased and 731 mouse-increased genes (Extended Data Fig. 3k), respectively. In SMCs, the human-increased genes included *PICALM*, which is associated with Alzheimer's disease and involved in amyloid-β clearance through the brain vasculature[11], and the muscle-differentiation-associate d[12] long noncoding RNA *CARMN*.

Comparison of post mortem versus ex vivo samples revealed 232 tissue-source DEGs (tsDEGs) (1.34%) at the same threshold (8× fewer than mouse), and revealed many functional changes associated with ageing, as expected given the age difference between our samples (ex vivo average: 15.8 years; post mortem average: 86.8 years). Gene ontology analysis of tsDEGs included: decreased BBB maintenance and increased vascular endothelial growth factor (VEGF) signalling in pericytes and decreased cell–cell adhesion and membrane assembly in fibroblasts (Supplementary Table 3). Although these changes are consistent with known dysfunctions of the cerebrovasculature due to ageing[5], they could reflect differences in post mortem and ex vivo tissue quality.

Human-specific endothelium zonation

Brain endothelial cells show phenotypic zonation[4] along the arteriovenous axis. Although poorly understood, zonated characteristics arise in disease, including pathologies of small calibre arteries in cerebral arteriopathies[13], and capillaries in neurodegenerative disorders[6]. To profile human endothelial molecular zonation signatures, we developed a continuous quantitative measure of spatial cell positioning using a linear regression model, focusing specifically on ex vivo nuclei. We found 1,802 genes that exhibited a gradient of expression along the arteriovenous axis, including 147 transcription factors and 76 transporters (Extended Data Fig. 4a, b), indicating a gradual transcriptional continuum (Fig. 3a, b). We found that human zonation (Fig. 3b) was conserved in a previous mouse dataset[4] (Extended Data Fig. 5a); however, the set of zonated genes highly diverged, with only a small subset of zonated genes conserved between species (≈10%) (Extended Data Fig. 5b). We found conservation between markers of human and mouse arterioles (*VEGFC*, *BMX* and *EFNB2*) and capillaries (*MFSD2A* and *TFRC*), but venule markers differed. For example, *SLC38A5* was expressed in both capillaries and venules in human, but only in venules in mouse. *TSHZ2* and *LRRC1* were both venule zonated in human, but showed no expression in mouse endothelium. We found that several transcription factors known to promote endothelial or arterial fate, including *HEY1* and *GATA2* (ref. [14]), are arteriole zonated, and also reveal several new venule-zonated transcription factors, including *TSHZ2*, *BNC2* and *ETV6*.

We experimentally validated the zonated expression of several genes using freshly resected cortical tissue, confirming human-specific capillary/venule zonation of *ANO2* (Fig. 3c), which lacks endothelial cell expression in mouse[2], human-specific venule zonation of *TSHZ2* (Extended Data Fig. 5c) and human–mouse-conserved[4] arteriole zonation of *VEGFC*. We also found human-specific expression of the metallothioneins *MT1E* and *MT2A* (Extended Data Fig. 5d, e) that show astrocytic but not vascular expression in mouse.

Differentially zonated genes were enriched in distinct gene ontologies and pathways (Fig. 3d and Extended Data Fig. 5f). For example, venule-zonated genes were enriched in interleukin signalling pathways, consistent with the central role of venules in leukocyte adhesion and

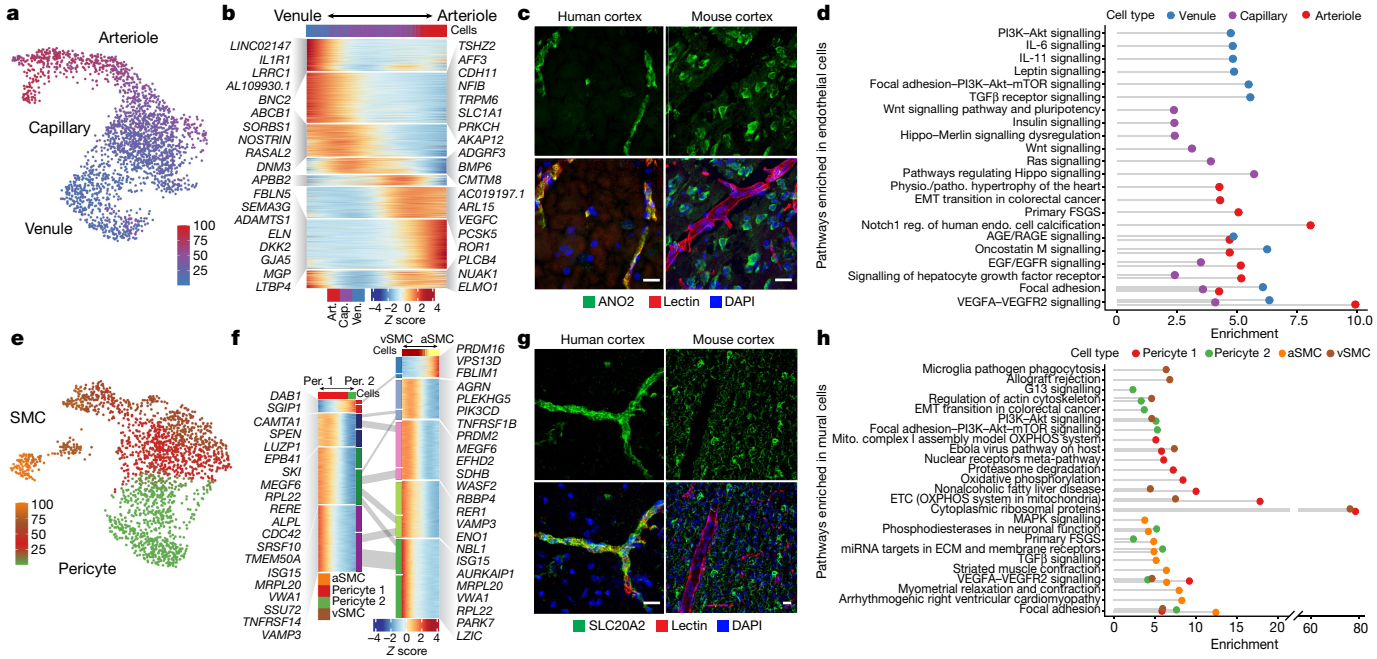

Fig. 3 | Molecular zonation of human brain endothelial and mural cells. **a**, Zonal gradient of endothelial cell transcriptomes (normalized pseudotime predicted from Monocle3 (range 1–100)). **b**, Genes expressed at higher levels along the endothelial gradient. Art., arteriole; cap., capillary; ven., venule. **c**, Indirect immunofluorescence of expression of the human endothelial marker ANO2, and its mouse homologue, in brain cortex. **d**, Pathway analysis along endothelial zones. Physio., physiological; patho., pathological; EMT, epithelial-to-mesenchymal transition; FSGS, focal segmental glomerulosclerosis; reg., regulation; endo., endothelial; AGE, advanced glycation endproduct; RAGE, receptor for AGE. **e**, Zonal gradient of mural cell transcriptomes (normalized pseudotime predicted from Monocle3 (range 1–100)). **f**, Genes expressed at higher levels along the mural gradients. Grey lines depict shared genes across gradients. Per., pericyte. **g**, Indirect immunofluorescence of the expression of the human mural marker SLC20A2, and its mouse homologue, in brain cortex. **h**, Pathway analysis along mural zones. Mito. mitochondrial; OXPHOS, oxidative phosphorylation; ETC, electron transport chain. Representative images in **c** and **g** shown from $n = 3$ independent biological replicates for each marker. Brightness and contrast enhanced for visualization. Scale bars, 20 µm.

cytokine release[15]. Arterial-zonated genes were enriched in Notch signalling, consistent with the role of Notch alterations in arteriopathies[13]. These results show that although zonated functional organization is a conserved characteristic across species, the human cerebrovasculature exhibits a species-specific gene expression pattern.

Human mural cell molecular zonation

Studies of mural cells have elucidated distinct morphologies along the vasculature[16], but they remain poorly defined at the molecular level. We found that unlike endothelial cells, mural cells exhibit two distinct and separate transcriptional gradients for pericytes and SMCs, regardless of their position along the arteriovenous axis (Fig. 3e) and not previously observed in mice[4]. In total, we identified 1,820 zonated genes in pericytes (Extended Data Fig. 6a, b) and 2,756 in SMCs (Extended Data Fig. 7a, b) that exhibit distinguishable expression patterns (Fig. 3f). We found that the zonated genes in SMCs and pericytes are significantly shared. For example, the genes expressed at higher levels in pericyte 1 were enriched in vSMCs. By contrast, genes expressed at higher levels in pericyte 2 were expressed at higher levels in aSMCs (Fig. 3f and Extended Data Fig. 7c).

We found zonated expression of several apolipoproteins in vSMCs, including those encoded by *APOD*, *APOE* and *APOO*. Failure of amyloid-β clearance in the perivenous space is thought to contribute to cerebral amyloid angiopathy and deficits of perivenous drainage in Alzheimer's disease[17]. Given the localized recruitment of immune cells to venules, the zonated expression of apolipoproteins, in particular that encoded by *APOE*, by vSMCs suggests a zonated functional role of amyloid-β clearance. In addition, our analysis revealed the expression of specific genes in human mural cells. We validated the expression of *SLC20A2* and *SLC30A10* and demonstrated these mural- and human-specific genes to exhibit expression wrapped around vessels but not co-localized with the endothelial marker lectin (Fig. 3g and Extended Data Fig. 8a). In pericytes and SMCs, we validated the zonated expression of GRM8 (Extended Data Fig. 8b) and FRMD3 by co-staining with the known aSMC marker ACTA2 (Extended Data Fig. 8c, d). We observed FRMD3 expression on large ACTA2$^+$ vessels (Extended Data Fig. 8d), and on a subset of small microvessels with different morphologies, reminiscent of known pericyte heterogeneity. Furthermore, SLC20A2, SLC30A10, GRM8 and FRMD3 exhibited expression patterns in non-vascular cell types within the mouse posterior cortex, demonstrating the species-specific expression in human mural cells (Fig. 3g and Extended Data Fig. 8a–c).

Last, gene ontology and pathway analyses indicated that genes expressed at high levels in pericyte 2 and aSMCs were significantly enriched in SMC contraction and cardiac muscle cell action potential terms. Likewise, genes expressed at high levels in pericyte 1 and vSMC were significantly enriched in VEGF signalling pathway and immune responses terms (Fig. 3h and Extended Data Fig. 8e). The pathways enriched in pericyte 1 more closely resembled vSMCs, whereas pericyte 2 more closely resembled aSMCs, suggesting functional similarities between aSMC and pericyte 2 and between vSMC and pericyte 1. Together with gene expression profiling and immunostaining validation, our pathway analysis suggests that pericyte 2 represents the subclass of pericytes in closer proximity to arterioles, whereas pericyte 1 represents pericytes in closer proximity to venules.

Perivascular fibroblasts in human cortex

Endothelial cells, mural cells and astrocytes are notable components of the cerebrovasculature; however, recent studies in animal models

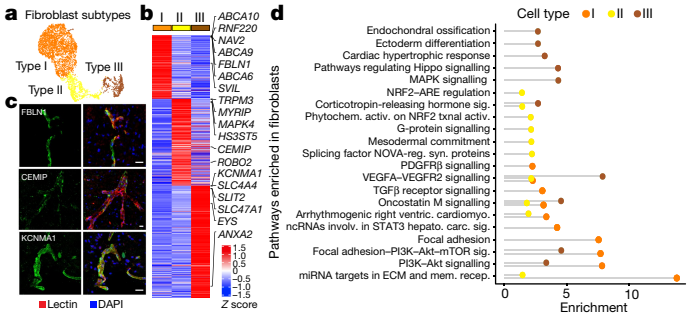

Fig. 4 | Perivascular fibroblasts in the human cerebrovasculature. a, UMAP of integrated perivascular fibroblast subtypes from human ex vivo and in silico-sorted brains. **b**, Genes expressed at high levels in fibroblast subtypes. **c**, Indirect immunofluorescence of expression of the fibroblast markers FBLN1, CEMIP and KCNMA1. **d**, Enriched pathway analysis in perivascular fibroblast subtypes. Sig., signalling; reg. regulated; syn. synaptic; ventric., ventricular; cardiomyo., cardiomyocytes; involv., involved; hepato., hepatocellular; carc., carcinoma; mem., membrane; recep., receptor; activ., activation; phytochem., phytochemical. Representative images in **c** from $n = 3$ independent biological replicates for each marker. Brightness and contrast enhanced for visualization. Scale bars, 20 µm.

have demonstrated a class of perivascular fibroblasts as being integral for vascular structure[2,4,18]. In particular, these perivascular fibroblasts, or stromal cells, express collagens and laminins, which are essential components of the extracellular matrix (ECM)[19] and contribute to fibrotic scar formation after injury to the central nervous system[20]. Distinct fibroblast subtypes are present in mouse cerebrovasculature[4,21]; however, the limited number has prevented characterization of their distinct transcriptional profiles and function.

In our analysis, we uncovered three distinct subtypes of perivascular fibroblasts (Fig. 4a), two of which were consistent with those identified in mouse (types I and II). Type III fibroblasts shared expression of the mouse arachnoid barrier cell (ABC) marker[21] *SLC47A1*; however, several other markers of ABCs are not expressed in type III fibroblasts. As we did not expect to have ABCs, the human type III fibroblasts revealed by our analysis probably constitute a new human fibroblast subtype. Nevertheless, all subtypes expressed specific sets of genes (Fig. 4b), some of which are also expressed in mouse brain fibroblasts, although subtype-specific expression had not previously been assessed. We confirmed protein level expression of *FBLN1*, *CEMIP* and *KCNMA1*, as markers for type I, II and III fibroblasts, respectively (Fig. 4c and Extended Data Fig. 9a).

Pathway and gene ontology enrichment analyses revealed distinct functional roles for each subtype (Fig. 4d and Extended Data Fig. 9b). Whereas all subtypes expressed genes involved in VEGF–VEGFR2 signalling, type I fibroblasts seem to be the main subtype involved in ECM organization. Given that fibrotic scars are predominantly composed of collagen I ECM protein[22], it is likely that type I fibroblasts are the contributing subtype to fibrosis during injury to the central nervous system. Type II and type III showed greater significance in pathways related to cell fate, with type III showing expression of various growth factors, including that encoded by *VEGFA*. Pseudotime analysis of ex vivo fibroblasts revealed two gradients of gene expression from type I to type II and to type III, separately (Extended Data Fig. 9c). The type I to type II trajectory was continuous with pericyte 2 (Extended Data Fig. 9d), suggesting a lineage from type I to type II to pericytes and consistent with a study demonstrating the stem cell potential of fibroblasts to differentiate into pericytes[18]. This is in line with our evidence that the pericyte 2 type cells are in closer proximity to arterioles given that fibroblasts have been shown to be localized predominantly at the level of penetrating arterioles[23]. Therefore, type II fibroblasts probably represent an intermediate state exhibiting a transitional mural cell transcriptional phenotype.

HD vascular dysfunction

Several studies have noted cerebrovascular abnormalities across neurodegenerative diseases, which often precede more disease-specific pathological features[6]. HD and HD-like syndromes including neuroferritinopathy[24] and primary familial brain calcification[25] are autosomal-dominant neurodegenerative diseases caused by mutations in either the *HTT* gene[26] or in the vasculature-expressed genes *FTH1* (ref. [24]) and *SLC20A2*, *PDGF* and *PDGFRB* (ref. [25]), respectively. In HD these abnormalities include increased BBB permeability, increased small vessel density, altered vessel morphology/cerebral blood volume, and activation of pericytes[27–30]. Although these changes have been shown to occur before the onset of HD-like phenotypes in the R6/2 (refs. [31,32]) and zQ175 (ref. [33]) mouse models and also in pre-symptomatic stages of HD[28,29], the molecular bases of these alterations are not well understood.

To study cerebrovascular cells in the context of disease, we re-annotated 2,198 cells from our previously published post mortem neostriatal HD samples[9], and studied their gene expression changes. We corrected the annotation of 895 fibroblasts that we had previously[9] identified as mural cells (Extended Data Fig. 10a–c). We also profile 1,747 additional cells from HD grade 1–4 and control cells purified with the BVE protocol on matched tissue samples from the caudate nucleus and putamen. Highlighting the importance of glia–vasculature cell interactions, we found that genes expressed at high levels in one subcluster of astrocytes and one subcluster of microglia were significantly enriched in regulation of angiogenesis and blood vessel endothelial cell migration, suggesting that these glial cells may be specified functionally for vasculature regulation (Extended Data Fig. 10d, e). The numbers of astrocytes and microglia were significantly increased (Fig. 5a), suggesting that astrocytes and microglial cells associate more closely with the vasculature in HD.

We found 4,698 HD DEGs (hdDEGs) between control and HD for endothelial, mural and fibroblast cell types (Supplementary Table 4), some of which are known to be dysregulated in neurodegenerative conditions, including *ABCB1*, *ABCG2* and *SLC2A1* downregulation in endothelial cells. *PDGFRB*, *SLC20A2* and *FTH1* were all significantly downregulated in mural cells. Mutations in these genes are known to cause HD-like syndromes with primary pathology localized in the basal ganglia[24,25], suggesting a link between vascular changes and regional vulnerability in HD. We also found significant endothelial downregulation of *MFSD2A*, which encodes a lipid transporter expressed in brain endothelial cells that restricts caveolae-mediated transcytosis[34], suggesting that its dysregulation may underlie increased vesicular trafficking and BBB leakage. In addition, endothelial HD cells showed upregulation of genes associated with sprouting angiogenesis, endothelial cell migration and VEGF signalling (Supplementary Table 4), changes that may underlie the increased vessel density reported in ref. [27]. We predicted upstream regulators of hdDEGs using chromatin enrichment analysis (Methods) and found that *TCF4*, a regulator of the Wnt pathway, was both a top predicted regulator in HD endothelial cells, and itself upregulated in endothelial cells (Supplementary Table 4 and Extended Data Fig. 10f). Consistent with this, the Wnt signalling pathway is upregulated in brain endothelial cell studies using induced pluripotent stem cells derived from patients with HD[35].

HD-upregulated genes in endothelial cells were enriched for many innate immune activation genes (Extended Data Fig. 10g), complementing our observation of innate immune activation in HD neostriatal spiny projection neurons[9], and being of interest given links between BBB dysregulation and innate immune activation[36]. Indeed, several key mediators of innate immune activation were upregulated in endothelial cells, including *IKBKB*, *IRF2/3* and *STAT3* (Supplementary Table 4). We found that innate immune activation genes were also significantly upregulated in HD for both astrocytes and microglia, including *IRF3* and *TRAF3* (Supplementary Table 5). To validate this upregulation of

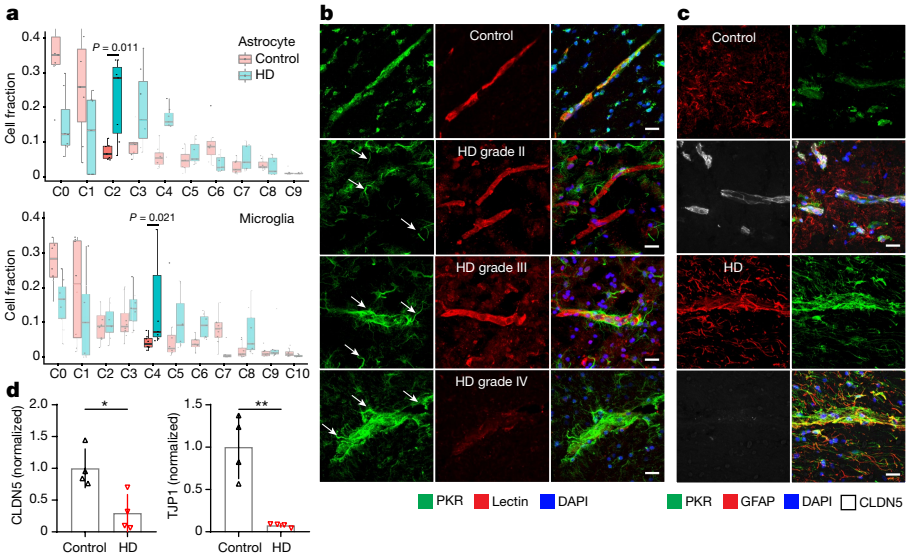

Fig. 5 | Innate immune activation related to cerebrovascular dysfunction in HD. a, Cell fraction analysis of astrocyte (C0–C9) and microglia (C0–C10) subclusters; *P* value shown for highlighted clusters is calculated using the Wilcoxon rank sum test ($n = 8$ for each group). Centre line denotes the median; box limits denote the upper and lower quartiles; and whiskers denote the 1.5× interquartile range; dots denote individuals. **b**, PKR immunostaining in perivascular glial processes across various HD grades. PKR is normally detected in the vasculature in control samples; arrows indicate PKR-immunopositive glial processes that become apparent only in HD samples. **c**, PKR immunostaining co-localizes with GFAP and engulfs blood vessels with low expression levels of CLDN5. **d**, Western blot quantification for the tight junction proteins CLDN5 (left) and TJP1 (right). Two-tailed *t*-test, $^{*}P = 0.0158$, $^{**}P = 0.0025$. Error bars denote s.d. of the mean from $n = 4$ biologically independent samples from the caudate nucleus of controls and patients with HD. Representative images in **b** and **c** from $n = 3$ independent biological replicates for each immunostaining experiment. Brightness and contrast enhanced for visualization. Scale bars, 20 µm.

innate immune signalling in astrocytes and microglia, we assessed expression of the innate immune sensor PKR in HD and HD mouse model tissue. In control tissue, some PKR expression is normally seen in the cerebrovasculature. We observed strong PKR upregulation in what seemed to be glial processes that engulfed blood vessels, in both human HD (Fig. 5b) and R6/2 HD mouse model samples (Extended Data Fig. 10h). These engulfed blood vessels were devoid of, or exhibited low levels of, the BBB tight junction protein CLDN5, and the engulfing processes were immunopositive for the astrocyte marker glial fibrillary acidic protein (GFAP), suggesting a correlation between endothelial and glial cell innate immune activation and a reduction of endothelial tight junction protein levels (Fig. 5c and Extended Data Fig. 10h). We further confirmed a significant reduction to overall levels of the BBB tight junction proteins CLDN5 and TJP1 (Fig. 5d and Extended Data Fig. 10i). As downregulation of CLDN5 and TJP1 levels is known to lead to the loss of BBB integrity, taken together these data provide evidence for a co-occurrence of activation of innate immune signalling in endothelial cells/glial cells interacting with the vasculature and the loss of BBB integrity noted in HD.

Discussion

Interrogating cell types of the cerebrovasculature in humans at a molecular level has been challenging owing to a lack of a high-throughput methodology to capture these cell types for genome-wide gene expression analyses. Species-specific patterns of expression between mouse and human brain microvessels have been noted, but the lack of cellular specificity has prevented a thorough mapping of their molecular composition[37]. Here, by developing independent experimental and in silico sorting methodologies for the enrichment and compatibility with snRNA-seq, we catalogued the transcriptional profiles of thousands of single nuclei comprising the human cerebrovasculature. Included are profiles generated from fresh human cortex surgical resections that eliminate any possibility of transcriptional alterations associated with the post mortem interval. These profiles reveal human-specific characteristics of the cerebrovasculature. We observe that vascular zonation is an evolutionarily conserved phenomenon when comparing mice to humans despite notable gene expression differences along the arteriovenous axis. We observed similar degrees of diversity and specificity in the gene expression patterns of mural cells, which until now have remained ill-defined, and validated the expression of new marker genes, confirming the cell-type-specific expression at the protein level. In addition, we identified three subtypes of perivascular fibroblasts. Last, in our ex vivo enriched dataset, we found subpopulations of neuronal and glial cells co-clustering with vascular cell types. We excluded these cells from analysis here, owing to the possibility of nuclei doublets, but they may represent bona fide populations of vasculature-coupled cells, as recently reported for both microglia and adult-born immature neurons[38,39], and future work will be needed to elucidate their identity and functions.

Understanding the normal cellular and molecular characteristics of the cerebrovasculature is crucial for studying mechanisms of its dysfunction. Thus, we also conducted cell-type-specific differential gene analysis of cerebrovascular cells in the context of HD to elucidate potential mechanisms of dysfunction. In addition to the previously studied Wnt signalling pathway[35], our work reveals the activation of the innate immune signalling, which we have recently reported to occur in striatal neurons[9,35], as also occurring in endothelial cells and vascular-interacting astroglial and microglial cells in the HD brain. Our work reveals that this innate immune activation co-occurs with loss of endothelial tight junction protein expression, suggesting that blockade of innate immune activation in the HD brain could prevent loss of BBB integrity. Future studies in mouse models will provide further insights into the therapeutic potential of targeting these gene alterations in the cerebrovasculature. Further investigating large intracranial vessels will be of great importance given their prominent role in other neurological diseases[40].

Online content

Any methods, additional references, Nature Research reporting summaries, source data, extended data, supplementary information, acknowledgements, peer review information; details of author contributions and competing interests; and statements of data and code availability are available at https://doi.org/10.1038/s41586-022-04521-7.

1. Sweeney, M. D., Zhao, Z., Montagne, A., Nelson, A. R. & Zlokovic, B. V. Blood-brain barrier: from physiology to disease and back. *Physiol. Rev.* **99**, 21–78 (2019).
2. Saunders, A. et al. Molecular diversity and specializations among the cells of the adult mouse brain. *Cell* **174**, 1015–1030 (2018).
3. Sabbagh, M. F. et al. Transcriptional and epigenomic landscapes of CNS and non-CNS vascular endothelial cells. *eLife* **7**, e36187 (2018).
4. Vanlandewijck, M. et al. A molecular atlas of cell types and zonation in the brain vasculature. *Nature* **554**, 475–480 (2018).
5. Montagne, A. et al. Blood-brain barrier breakdown in the aging human hippocampus. *Neuron* **85**, 296–302 (2015).
6. Sweeney, M. D., Kisler, K., Montagne, A., Toga, A. W. & Zlokovic, B. V. The role of brain vasculature in neurodegenerative disorders. *Nat. Neurosci.* **21**, 1318–1331 (2018).
7. Lee, Y.-K., Uchida, H., Smith, H., Ito, A. & Sanchez, T. The isolation and molecular characterization of cerebral microvessels. *Nat. Protoc.* **14**, 3059–3081 (2019).
8. Mathys, H. et al. Single-cell transcriptomic analysis of Alzheimer's disease. *Nature* **570**, 332–337 (2019).
9. Lee, H. et al. Cell type-specific transcriptomics reveals that mutant Huntingtin leads to mitochondrial RNA release and neuronal innate immune activation. *Neuron* **107**, 891–908 (2020).
10. Bennett, D. A. et al. Religious Orders Study and Rush Memory and Aging Project. *J. Alzheimer's Dis.* **64**, S161–S189 (2018).
11. Zhao, Z. et al. Central role for PICALM in amyloid-β blood-brain barrier transcytosis and clearance. *Nat. Neurosci.* **18**, 978–987 (2015).
12. Lim, Y.-H. et al. Identification of long noncoding RNAs involved in muscle differentiation. *PLoS ONE* **13**, e0193898 (2018).
13. Joutel, A. et al. *Notch3* mutations in CADASIL, a hereditary adult-onset condition causing stroke and dementia. *Nature* **383**, 707–710 (1996).
14. Park, C., Kim, T. M. & Malik, A. B. Transcriptional regulation of endothelial cell and vascular development. *Circ. Res.* **112**, 1380–1400 (2013).
15. Ley, K., Laudanna, C., Cybulsky, M. I. & Nourshargh, S. Getting to the site of inflammation: the leukocyte adhesion cascade updated. *Nat. Rev. Immunol.* **7**, 678–689 (2007).
16. Attwell, D., Mishra, A., Hall, C. N., O'Farrell, F. M. & Dalkara, T. What is a pericyte? *J. Cereb. Blood Flow Metab.* **36**, 451–455 (2016).
17. Morrone, C. D., Bishay, J. & McLaurin, J. Potential role of venular amyloid in Alzheimer's disease pathogenesis. *Int. J. Mol. Sci.* **21**, 1985 (2020).
18. Rajan, A. M., Ma, R. C., Kocha, K. M., Zhang, D. J. & Huang, P. Dual function of perivascular fibroblasts in vascular stabilization in zebrafish. *PLoS Genet.* **16**, e1008800 (2020).
19. Muhl, L. et al. Single-cell analysis uncovers fibroblast heterogeneity and criteria for fibroblast and mural cell identification and discrimination. *Nat. Commun.* **11**, 3953 (2020).
20. Fernández-Klett, F. et al. Early loss of pericytes and perivascular stromal cell-induced scar formation after stroke. *J. Cereb. Blood Flow Metab.* **33**, 428–439 (2013).
21. Zeisel, A. et al. Molecular architecture of the mouse nervous system. *Cell* **174**, 999–1014 (2018).
22. Dorrier, C. E. et al. CNS fibroblasts form a fibrotic scar in response to immune cell infiltration. *Nat. Neurosci.* **24**, 234–244 (2021).
23. Bonney, S. K., Sullivan, L. T., Cherry, T. J., Daneman, R. & Shih, A. Y. Distinct features of brain perivascular fibroblasts and mural cells revealed by in vivo two-photon imaging. *J. Cereb. Blood Flow Metab.*, https://doi.org/10.1177/0271678X211068528 (2021).
24. Chinnery, P. F. et al. Clinical features and natural history of neuroferritinopathy caused by the *FTL1* 460InsA mutation. *Brain* **130**, 110–119 (2007).
25. Tadic, V. et al. Primary familial brain calcification with known gene mutations. *JAMA Neurol.* **72**, 460–467 (2015).
26. MacDonald, M. E. et al. A novel gene containing a trinucleotide repeat that is expanded and unstable on Huntington's disease chromosomes. *Cell* **72**, 971–983 (1993).
27. Drouin-Ouellet, J. et al. Cerebrovascular and blood–brain barrier impairments in Huntington's disease: potential implications for its pathophysiology. *Ann. Neurol.* **78**, 160–177 (2015).
28. Chen, J. J., Salat, D. H. & Rosas, H. D. Complex relationships between cerebral blood flow and brain atrophy in early Huntington's disease. *Neuroimage* **59**, 1043–1051 (2012).
29. Harris, G. J. et al. Reduced basal ganglia blood flow and volume in pre-symptomatic, gene-tested persons at-risk for Huntington's disease. *Brain* **122**, 1667–1678 (1999).
30. Hua, J., Unschuld, P. G., Margolis, R. L., van Zijl, P. C. M. & Ross, C. A. Elevated arteriolar cerebral blood volume in prodromal Huntington's disease. *Mov. Disord.* **29**, 396–401 (2014).
31. Di Pardo, A. et al. Impairment of blood–brain barrier is an early event in R6/2 mouse model of Huntington disease. *Sci Rep.* **7**, 41316 (2017).
32. Padel, T. et al. Brain pericyte activation occurs early in Huntington's disease. *Exp. Neurol.* **305**, 139–150 (2018).
33. Liu, H. et al. Huntingtin silencing delays onset and slows progression of Huntington's disease: a biomarker study. *Brain* **144**, 3101–3113 (2021).
34. Ben-Zvi, A. et al. Mfsd2a is critical for the formation and function of the blood–brain barrier. *Nature* **509**, 507–511 (2014).
35. Lim, R. G. et al. Huntington's disease iPSC-derived brain microvascular endothelial cells reveal WNT-mediated angiogenic and blood-brain barrier deficits. *Cell Rep.* **19**, 1365–1377 (2017).
36. Daniels, B. P. & Klein, R. S. Viral sensing at the blood–brain barrier: new roles for innate immunity at the CNS vasculature. *Clin. Pharmacol. Ther.* **97**, 372–379 (2015).
37. Song, H. W. et al. Transcriptomic comparison of human and mouse brain microvessels. *Sci Rep.* **10**, 12358 (2020).
38. Mondo, E. et al. A developmental analysis of juxtavascular microglia dynamics and interactions with the vasculature. *J. Neurosci.* **40**, 6503–6521 (2020).
39. Fujioka, T., Kaneko, N. & Sawamoto, K. Blood vessels as a scaffold for neuronal migration. *Neurochem. Int.* **126**, 69–73 (2019).
40. Wingo, A. P. et al. Shared proteomic effects of cerebral atherosclerosis and Alzheimer's disease on the human brain. *Nat. Neurosci.* **23**, 696–700 (2020).
41. Butler, A., Hoffman, P., Smibert, P., Papalexi, E. & Satija, R. Integrating single-cell transcriptomic data across different conditions, technologies, and species. *Nat. Biotechnol.* **36**, 411–420 (2018).
42. McGinnis, C. S., Murrow, L. M. & Gartner, Z. J. DoubletFinder: doublet detection in single-cell RNA sequencing data using artificial nearest neighbors. *Cell Syst.* **8**, 329–337 (2019).
43. Wang, D. et al. Comprehensive functional genomic resource and integrative model for the human brain. *Science* **362**, eaat8464 (2018).
44. Finak, G. et al. MAST: a flexible statistical framework for assessing transcriptional changes and characterizing heterogeneity in single-cell RNA sequencing data. *Genome Biol.* **16**, 278 (2015).
45. Chen, E. Y. et al. Enrichr: interactive and collaborative HTML5 gene list enrichment analysis tool. *BMC Bioinform.* **14**, 128 (2013).
46. Xie, Z. et al. Gene set knowledge discovery with Enrichr. *Curr. Protoc.* **1**, e90 (2021).
47. Kuleshov, M. V. et al. Enrichr: a comprehensive gene set enrichment analysis web server 2016 update. *Nucleic Acids Res.* **44**, W90–W97 (2016).
48. Ashburner, M. et al. Gene Ontology: tool for the unification of biology. *Nat. Genet.* **25**, 25–29 (2000).
49. The Gene Ontology Consortium. The Gene Ontology resource: 20 years and still GOing strong. *Nucleic Acids Res.* **47**, D330–D338 (2019).
50. Cao, J. et al. The single-cell transcriptional landscape of mammalian organogenesis. *Nature* **566**, 496–502 (2019).
51. Mohammadi, S., Davila-Velderrain, J. & Kellis, M. A multiresolution framework to characterize single-cell state landscapes. *Nat. Commun.* **11**, 5399 (2020).
52. Ritchie, M. E. et al. limma powers differential expression analyses for RNA-sequencing and microarray studies. *Nucleic Acids Res.* **43**, e47 (2015).

Methods

Animal use

All animal experiments were approved by the MIT Committee on Animal Care. Mice were grouped housed with food and water provided ab libitum on a standard 12 h light/12 h dark cycle. Male 6-week-old C57BL/6J wild-type mice (Jackson Laboratories stock number 000664) were used for snRNA-seq and immunofluorescence experiments. Male 9-week-old B6CBA-Tg(HDexon1)62Gpb/1J mice (CAG repeat length 160 ± 5; Jackson Laboratories stock number 002810) and non-carrier controls were used for R6/2 experiments. No prior procedures were performed on any animal before experiments. Randomization and blinding of animals was not necessary in this study given the unbiased experimental approach. All brain dissections were performed on dry ice after cooling the head in liquid nitrogen for 3 s. Dissected whole brain or posterior cortex were subsequently flash frozen in liquid nitrogen and stored at −80 °C until further use.

Human tissue

Human tissue analyses were conducted as exempt human research, as this was secondary research using biological specimens not specifically collected for this study. All samples were obtained from biobanks/repositories as follows, using appropriate de-identification and under consent. All resected ex vivo human tissue was originally obtained fresh or fresh-frozen from the Boston Children's Hospital through the Phenotyping and Banking Core of Neurological Disorders (protocol 09-02-0043 approved by the Boston Children's Hospital Institutional Review Board (IRB), under which samples are collected for the use of Boston Children's Hospital investigators and their collaborators). On surgical resection, tissue was examined by a licensed neuropathologist and allocated for clinical or research purposes. Non-pathologically deemed tissue was then either used immediately or stored fresh frozen at −80 °C until further use. All selected samples were from patients aged between 11 and 22 years with a primary diagnosis of medically refractory epilepsy with no known genetic mutations (that is, spontaneous epilepsy). Individuals with known arteriovenous malformations were also excluded from the study. In silico data were derived from 12 pathologically normal donor samples obtained from the Religious Orders Study and Rush Memory and Aging Project (ROSMAP), and data were obtained from the Rush Alzheimer's Disease Center Repository following guidelines approved by the IRB of the Rush University Medical Center. For these samples, all participants signed a Repository Consent form in addition to Informed Consent and an Anatomic Gift Aid. These ROSMAP samples included 7 brain regions: prefrontal cortex, mid-temporal cortex, angular gyrus, entorhinal cortex, thalamus, hippocampus and mammillary body. HD profiling data were derived from 8 HD and 8 age-matched unaffected control post mortem tissue samples, which were acquired through the National Institutes of Health (NIH) NeuroBioBank or the University of Alabama at Birmingham.

Indirect immunofluorescence staining

Brain tissue was collected from the HD R6/2 model and the control mice following transcardial perfusion with 4% PFA in 1× PBS. Human and mouse brain tissue samples were cryoprotected and cryosectioned onto glass slides at 20 µm thickness. Sections were fixed for 10 min using cold acetone (human alone) under gentle agitation, washed with 1× TBS, permeabilized with 1× TBS-T (1× TBS with 0.05% Tween20) and blocked with blocking buffer (2% heat-inactivated donkey serum, 0.1% fish gelatin in 1× TBS-T) for 1 h at room temperature. Slides were subsequently incubated with primary antibody in blocking buffer at specified dilutions (Supplementary Table 6) overnight at 4 °C. Slides were then washed with 1× TBS-T, incubated with secondary antibody (1:5,000 dilution of specified fluorophore as described in Supplementary Table 6) in blocking buffer for 1 h at room temperature, washed again with 1× TBS-T followed by 1× TBS, stained with DAPI and mounted with ProLong Gold antifade mounting medium (ThermoFisher Scientific). For post mortem human tissue sections, autofluorescent signal arising from endogenous lipofuscin was quenched with a 30-s exposure to TrueBlack Lipofuscin Autofluorescence Quencher (Biotium) and washed with 1× -TBS before mounting. A Zeiss LSM700 or LSM900 confocal microscope (Carl Zeiss AG) with a 20× and 40× objective lens was used for imaging. All image processing was performed using ImageJ software.

BVE for snRNA-seq

The BVE protocol was adapted from refs. [7,8]. All procedures were performed on ice. Ex vivo human, post mortem human and dissected mouse cortical tissue were homogenized in 5 ml MCDB 131 medium containing 0.5% (wt/vol) endotoxin-, fatty-acid- and protease-free BSA and 10 U µl^{-1} recombinant RNase Inhibitors using ten strokes with the loose pestle followed by ten strokes with the tight pestle in a 7-ml KIMBLE Dounce tissue grinder. Homogenized tissue was transferred into 15-ml conical tubes and centrifuged at 2,000*g* for 5 min at 4 °C using a fixed-angle rotor. Cell pellet was resuspended in 2 ml 17% (wt/vol) 70-kDa dextran solution (in 1× PBS + 10 U µl^{-1} recombinant RNase Inhibitors) and ultracentrifuged at 10,000*g* for 15 min at 4 °C in a swing-bucket rotor. Myelin and cellular debris were carefully removed before decanting supernatant. Resultant pellet or fresh-frozen tissue was homogenized in 700 µl homogenization buffer (320 mM sucrose, 5 mM $CaCl_2$, 3 mM $Mg(CH_3COO)_2$, 10 mM Tris HCl pH 7.8, 0.1 mM EDTA pH 8.0, 0.1% NP-40, 1 mM β-mercaptoethanol and 0.4 U µl^{-1} SUPERase In RNase Inhibitor (ThermoFisher Scientific)) with a 2-ml KIMBLE Dounce tissue grinder (MilliporeSigma) using ten strokes with the loose pestle followed by ten strokes with the tight pestle. Homogenized tissue was filtered through a 40-µm cell strainer and mixed with 450 µl of working solution (50% OptiPrep density gradient medium (MilliporeSigma), 5 mM $CaCl_2$, 3 mM $Mg(CH_3COO)_2$, 10 mM Tris HCl pH 7.8, 0.1 mM EDTA pH 8.0 and 1 mM β-mercaptoethanol). The mixture was then slowly pipetted onto the top of an OptiPrep density gradient containing 750 µl of 30% OptiPrep Solution (134 mM sucrose, 5 mM $CaCl_2$, 3 mM $Mg(CH_3COO)_2$, 10 mM Tris HCl pH 7.8, 0.1 mM EDTA pH 8.0, 1 mM β-mercaptoethanol, 0.04% NP-40 and 0.17 U µl^{-1} SUPERase In RNase Inhibitor) on top of 300 µl of 40% OptiPrep Solution (96 mM sucrose, 5 mM $CaCl_2$, 3 mM $Mg(CH_3COO)_2$, 10 mM Tris HCl pH 7.8, 0.1 mM EDTA pH 8.0, 1 mM β-mercaptoethanol, 0.03% NP-40 and 0.12 U µl^{-1} SUPERase In RNase Inhibitor) inside a Sorenson Dolphin microcentrifuge tube (MilliporeSigma). Nuclei were pelleted at the interface of the OptiPrep density gradient by centrifugation at 10,000*g* for 5 min at 4 °C using a fixed-angle rotor (FA-45-24-11-Kit). The nuclear pellet was collected by aspirating ≈100 µl from the interface and transferring to a 2.5-ml low-binding Eppendorf tube. The pellet was washed with 2% BSA (in 1× PBS) containing 10 µl^{-1} SUPERase In RNase Inhibitor. The nuclei were pelleted by centrifugation at 300*g* for 3 min at 4 °C in a swing-bucket rotor (S-24-11-AT). Nuclei were washed two times with 2% BSA and centrifuged under the same conditions. The nuclear pellet was then resuspended in ≈100 µl of 2% BSA and manually counted using a haemocytometer and microscope as well as being inspected for cellular debris.

Quantitative real-time PCR

Mouse posterior cortex was disrupted for RNA isolation using the TissueLyser (QIAGEN) for 2 × 2 min at 20 Hz as recommended by the manufacturer. Enriched blood vessel pellets from the BVE protocol were disrupted using QIAGEN Buffer RLT. RNA was then isolated using the RNeasy Lipid Tissue Mini Kit (QIAGEN). For qRT–PCR, the TaqMan Universal Master Mix (ThermoScientific) was used, and PCR reactions were run on a StepOnePlus system (ThermoScientific).

Western blotting

Human post mortem caudate nucleus tissue samples from patients with HD and age-matched unaffected controls were homogenized in 1 ml RIPA lysis buffer (ThermoScientific) containing a protease inhibitor

cocktail (MilliporeSigma). Approximately 10 μg of protein in 1× LDS was loaded onto 4–12% Bis-Tris gels and run using MOPS Running Buffer at 175 V for 1 h. Protein samples were then transferred onto PVDF membranes (Bio-Rad) using 10% methanol in 1× transfer buffer at 50 V for 1.5 h. Membranes were then washed in 1× TBS-T (1× TBS with 0.05% Tween20), blocked with 5% milk for 1 h at room temperature, and subsequently incubated with primary antibodies (Supplementary Table 6) in 5% milk at 4 °C overnight under gentle agitation. Membranes were then washed again with 1X TBS-T, and incubated with HRP secondary antibodies for 1 h at room temperature, and substrate (Pierce ECL Plus) was applied for chemiluminescent detection. Immunoblots were quantified using ImageJ software. Two-tailed paired *t*-tests were performed for statistical analysis.

snRNA-seq and associated analysis

Droplet-based snRNA-seq libraries were prepared using the Chromium Single Cell 3′ Reagent Kit v3 (10x Genomics) according to the manufacturer's protocol and sequenced on an Illumina NovaSeq6000 at the MIT BioMicro Center. Raw sequencing reads were aligned to the pre-mRNA annotated *Mus musculus* reference genome version GRCm38 or *Homo sapiens* reference genome version GRCh38 and counts were estimated using Cellranger 3.0.1 (10x Genomics). The generated cell-by-gene unique molecular identifier (UMI) count matrix was analysed using the Seurat R package v.3.2.0 (ref. [41]). We kept only the cells expressing at least 500 genes and genes with expression in at least 50 cells. The cells were also filtered by the maximum of 8,000 expressed genes and of 10% mitochondrial genes. The UMI counts were then normalized for each cell by the total expression, multiplied by 10,000 and log transformed. We used Seurat's default method to identify highly variable genes and scale data for regressing out variation from UMI and mitochondrial genes. The scaled data with variable genes were used to perform principal component analysis. The top 30 principal components were chosen for further analysis, including clustering to identify cell populations. UMAPs were calculated in the Seurat R package using the top 30 PCs and min_dist = 0.75. Harmony was used to perform batch-effect correction.

Doublet removal

To remove the potential doublets in the dataset, we first used DoubletFinder with the parameter of 7.5% doublet formation rate on the basis of the recommendation of 10x Genomics at the single-cell level to identify the most likely doublets[42]. Then, clusters of cells showing higher expression of marker genes corresponding to two or more cell types were excluded from further analysis.

Cell-type annotation and marker-gene identification

To annotate the cell type for each cluster, we identified the marker genes using the Wilcoxon rank sum test by comparing one cluster with the others. Next, we checked the canonical markers (excitatory neuron: *NRGN*, *SLC17A7* and *CAMK2A*; inhibitory neuron: *GAD1* and *GAD2*; astrocyte: *AQP4* and *GFAP*; oligodendrocyte: *MBP*, *MOBP* and *PLP1*; microglia: *CSF1R*, *CD74* and *C3*; oligodendrocyte precursor cell: *VCAN*, *PDGFRA* and *CSPG4*; endothelial: *FLT1* and *CLDN5*; pericyte: *AMBP*) in each cluster to determine the cell type. Finally, we performed gene set enrichment analysis by testing the significance of overlapping genes between marker genes that we identified and the published marker-gene sets[43] to further confirm the cell type of each cluster.

In silico sorting approach

For the full snRNA-seq datasets with all cell types in the brain (excitatory and inhibitory neurons, astrocytes, oligodendrocytes, oligodendrocyte precursor cells, microglia and vascular cells), we first performed clustering and annotated the cell type for each cluster on the basis of the canonical markers of vascular cell types and then calculated the cell-type score for each cell on the basis of the average expression of a set of vascular markers[43]. The cells with the specific high score of vascular cell types were kept for further integrative analysis (twofold higher than the second score).

Integrative analysis of human fresh, frozen and mouse single-cell RNA-seq datasets

The homologue genes of human and mouse were kept for integration. Canonical correlation analysis in Seurat[41] was used to integrate human snRNA-seq data from fresh and frozen samples and mouse single-cell RNA-seq data[4]. To compare the difference between human fresh and frozen samples, we applied MAST in R to identify the DEGs (tsDEGs) by considering age and sex as the covariates[44]. We used the Wilcoxon rank sum test to identify the DEGs between human and mouse data (two comparisons: human fresh versus mouse; human frozen versus mouse) and tested the significance of agreement between two comparisons by Fisher's exact test.

Functional enrichment analysis

Enrichr in R (refs. [45–47]) was used to perform functional enrichment analysis based on the following databases: Gene Ontology 2018 (refs. [48,49]), KEGG/WikiPathways 2019 Human and ChIP Enrichment Analysis 2016. False discovery rate (FDR) < 0.05 was used as a threshold to select the significant enrichment.

Endothelial and mural zonation analysis

The cell orders along the endothelial and mural zonation were determined by the pseudotime analysis using Monocle3 (ref. [50]). We next built a quadratic linear regression model to identify the zonation-related genes, smoothed the gene expression along the predicted zonation axis by fitting a smoothing spline in R, and clustered those genes into eight distinct expression patterns.

Differential gene expression analysis

We identified DEGs between control and HD samples (hdDEGs) using a multiresolution method in ACTIONet v2.1.9 (ref. [51]). In brief, the pseudobulk gene expression matrix for each sample is generated on the basis of a number of multiresolution bins (by default is 25). The single-cell variance in pseudobulk data is also considered as a covariate when limma[52] is applied for differential analysis. In addition, age, sex and PMI are also controlled as covariates in the model. Genes with FDR < 0.05 and $\log_2$[foldchange] > 0.05 were used for subsequent functional enrichment analysis as described above.

Reporting summary

Further information on research design is available in the Nature Research Reporting Summary linked to this paper.

Data availability

Count matrices for all cells analysed in this study have been uploaded with this submission at http://compbio.mit.edu/scBBB/. An interactive website is available at https://nsun.shinyapps.io/scbbb/. Raw sequencing data associated with Figs. 1–5 are available in the National Center for Biotechnology Information Gene Expression Omnibus under accession number GSE173731. Sample identifiers for ROSMAP and HD human tissue samples are listed in Supplementary Table 1. With these identifiers, data/sample acquisition for the HD samples can be accessed at https://neurobiobank.nih.gov/. ROSMAP samples and data can be accessed at https://www.radc.rush.edu. This website includes detailed documentation on variables and cross-calculations of selected variables, and the relevant Data Use Agreement and Material Transfer Agreement can also be downloaded from this site. Samples (and data regarding them) from the Boston Children's Hospital were collected for the use of Boston Children's Hospital investigators and their collaborators, and are not freely available. Further enquiries regarding these samples can be directed to the corresponding authors.

Code availability

The code used in this study is available at http://compbio.mit.edu/scBBB/. Code used in this study is also available upon reasonable request from the corresponding authors.

Acknowledgements This research was supported in part by the Intellectual and Developmental Disability Research Center (financed by NIH U54 HD090255 and P50 HD105351) and the Rosamund Stone Zander Translational Neuroscience Center at the Boston Children's Hospital (to M.S.), a Picower Institute Innovation Fund Award and a Walter B. Brewer (1940) MIT Fund Award (to M.H.), and NIH AG054012, AG058002, AG062377, NS110453, NS115064, AG067151, AG062335, MH109978, MH119509 and HG008155 and Cure Alzheimer's Fund CureAlz-CIRCUITS (to M.K.). ROSMAP was supported by National Institute on Aging grants P30AG10161, R01AG15819, R01AG17917 and U01AG61356. We thank A. H. Effenberger for assistance in graphics design; S. S. Pineda for assistance with differential gene expression analysis; P. Ge for assistance with the western blot experiments; and L.-L. Ho and Z. Peng, for collaborative and scientific input on experimental profiling. We also thank the NIH NeuroBioBank and the University of Alabama at Birmingham for providing the human HD and control samples used in this study.

Author contributions F.J.G. designed the human and mouse studies and developed the BVE protocol; N.S. conducted data analysis with assistance from F.J.G. and H.L.; B.G. and M.S. assisted in ex vivo human tissue sample acquisition; H.L. assisted with BVE snRNA-seq sample preparation; B.Z. performed vascular-related experiments and quantification; K.G. and J.M. conducted snRNA-seq post mortem sample profiling; H.M., X.J., A.P.N. and L.-H.T. provided pre-publication ROSMAP data; D.A.B. provided post mortem samples; F.J.G., N.S., M.K. and M.H. wrote the paper with comments from all authors; and M.K. and M.H. supervised the project.

Competing interests The authors declare no competing interests.

Additional information

Supplementary information The online version contains supplementary material available at https://doi.org/10.1038/s41586-022-04521-7.

Correspondence and requests for materials should be addressed to Manolis Kellis or Myriam Heiman.

Peer review information *Nature* thanks the anonymous reviewers for their contribution to the peer review of this work.

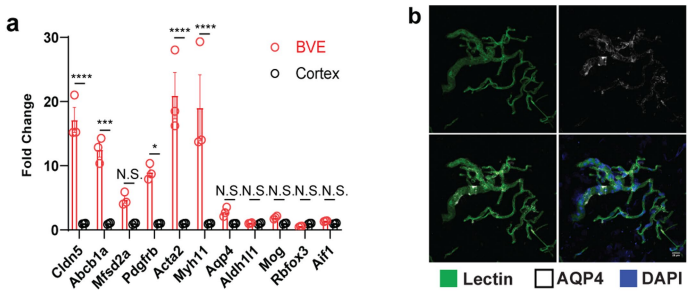

Extended Data Fig. 1 | Validation of Blood Vessel Enrichment (BVE) protocol. a. qPCR of canonical cell type markers for endothelial *Cldn5* ($p < 0.0001$), *Abcb1a* ($p = 0.0002$), *Mfsd2a* ($p = 0.9556$), mural *Pdgfrb* ($p = 0.0388$), *Acta2* ($p < 0.0001$), *Myh11* ($p < 0.0001$), astrocytes *Aqp4* ($p > 0.9999$), *Aldh1l1* ($p > 0.9999$), oligodendrocytes *Mog* ($p > 0.9999$), neurons *Rbfox3* ($p > 0.9999$), and microglia *Aif1* ($p > 0.9999$) from mouse cortex, ordinary one-way ANOVA, $^{*}p < 0.05$, $^{**}p < 0.01$, $^{***}p < 0.001$, $^{****}p < 0.0001$, n.s. = not significant. Error bars denote standard deviation of the mean from $n = 3$ independent biological replicates. **b**. Representative immunofluorescence of blood vessels enriched from mouse cortex using the BVE protocol. $n = 3$ independent biological replicates for immunostaining. Brightness and contrast enhanced for visualization. Scale bar, 20 µm.

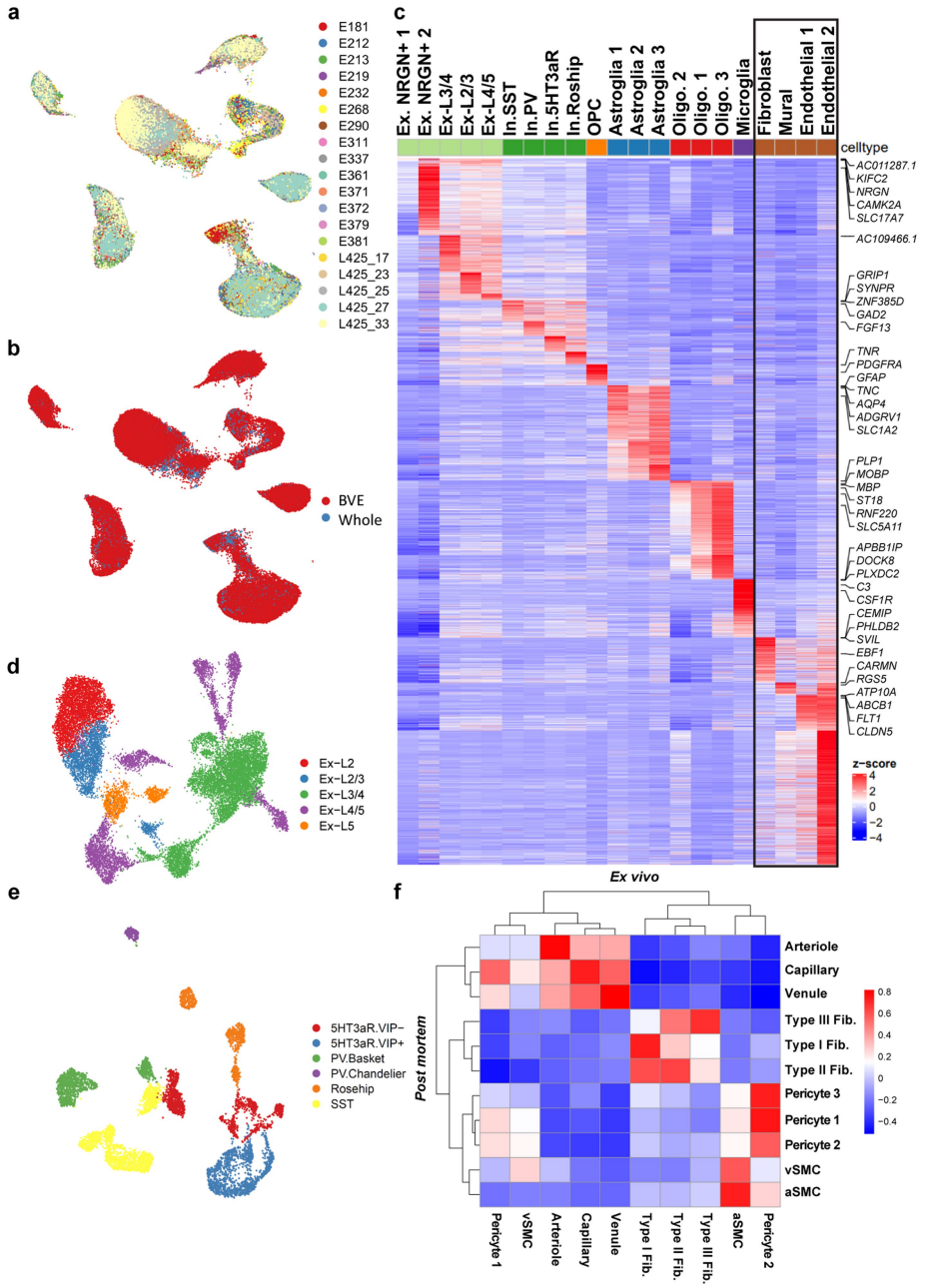

Extended Data Fig. 2 | Characterization of human snRNA-seq data from human temporal cortex. a. UMAP of *ex vivo* dataset by patient ID. **b**. UMAP of *ex vivo* dataset by experimental protocol. **c**. Heatmap of top cell-type differentially-expressed genes (ctDEGs) in major cell types from *ex vivo* human tissue. **d**. UMAP sub-clustering of excitatory neurons. **e**. UMAP sub-clustering of inhibitory neurons. **f**. Correlation heatmap between *ex vivo* and *post mortem* vascular cell types.

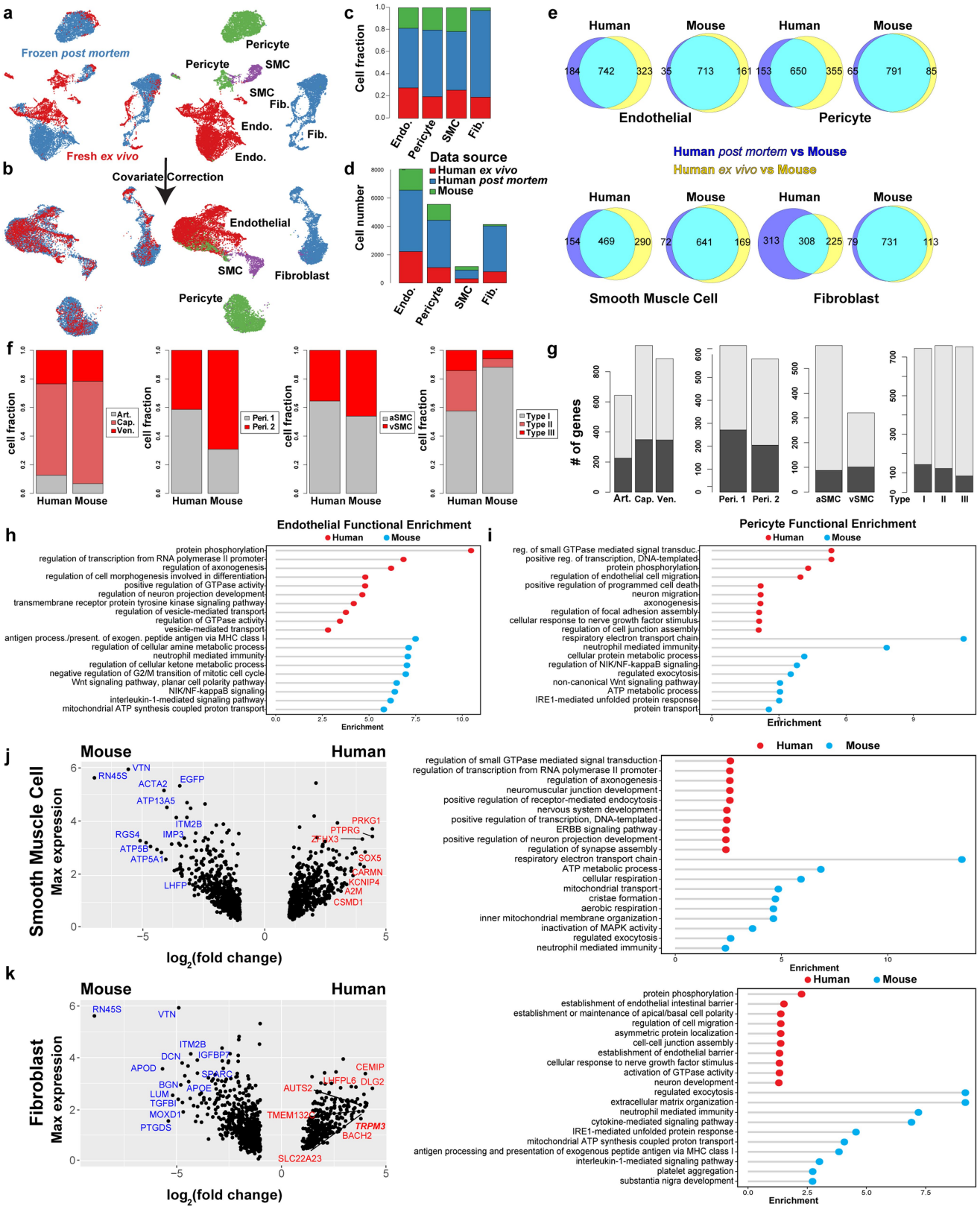

Extended Data Fig. 3 | See next page for caption.

Extended Data Fig. 3 | Integrative analysis of *ex vivo*, *post mortem*, and mouse datasets. a. UMAP plot of integrated human snRNA-seq datasets without covariate correction shown by platform and cell type and **b**. with covariate correction by platform and cell type **c**. Cell fraction distribution of single nuclei across all datasets by cerebrovasculature cell type. **d**. Cell number distribution of single nuclei across all datasets by cerebrovasculature cell type. **e**. Venn diagram overlap of genes between human *post mortem* vs. mouse and human *ex vivo* vs. mouse. **f**. Cell fraction and **g**. gene comparison of vascular cell types between mouse and human datasets. **h**–**i**. Representative functional enriched terms of human- and mouse-specific/highly expressed genes in endothelial (**h**) and pericytes (**i**). Human-mouse differentially expressed genes (hmDEGs) smooth muscle cells (**j, left**), and fibroblast (**k, left**). X-axis represents the log-transformed fold change and y-axis represents the maximal expression level. The top genes are highlighted in blue for mouse and red for human. Genes that were also cell type markers are bolded. **j**–**k. (right panels)**, the representative functional enriched terms of human- and mouse-specific/highly expressed genes.

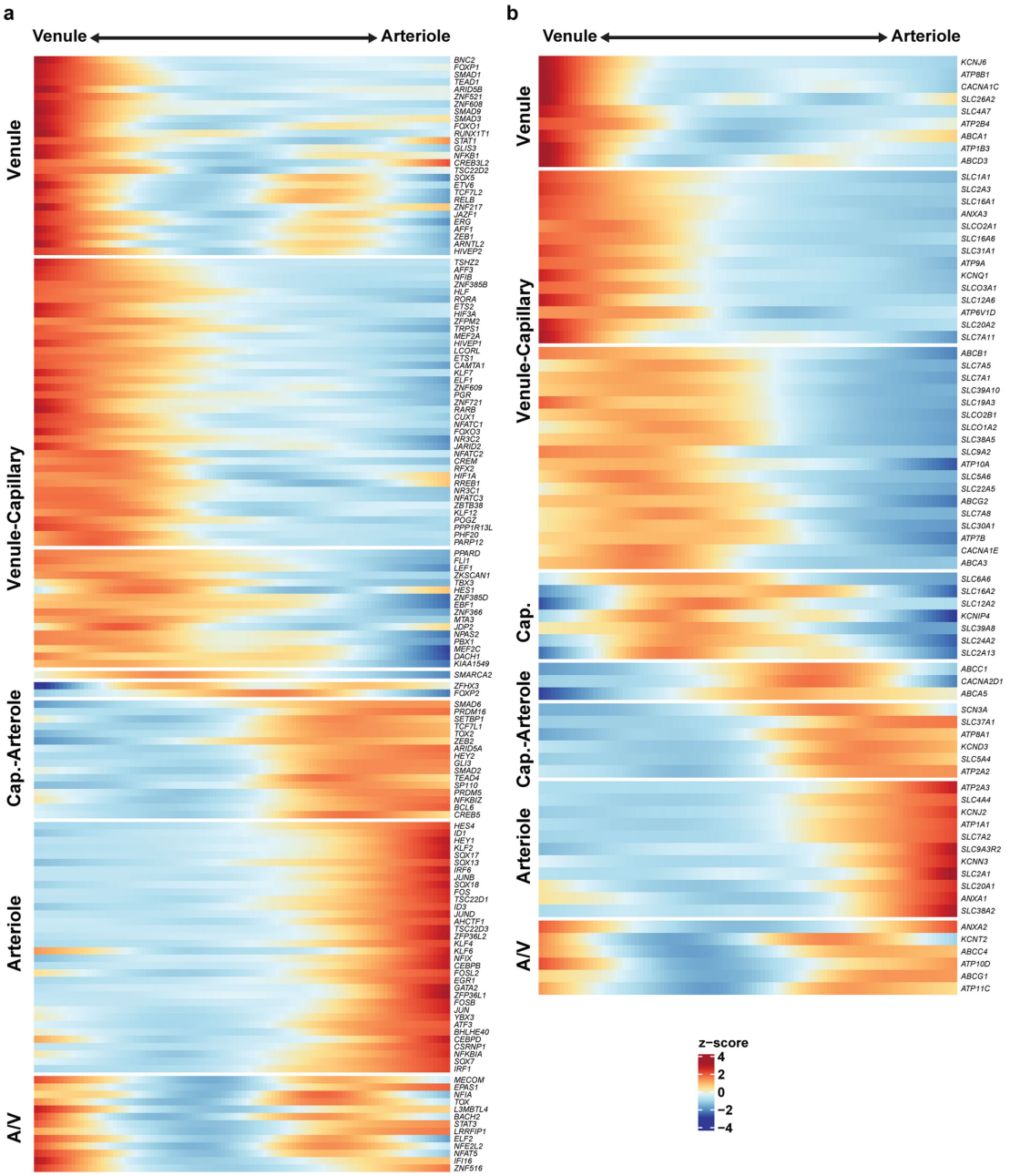

Extended Data Fig. 4 | Zonation gene expression analysis of human endothelial cells. a. Heatmap of 147 zonated transcription factors along the endothelial gradient. **b**. Heatmap of 76 zonated transporters along the endothelial gradient.

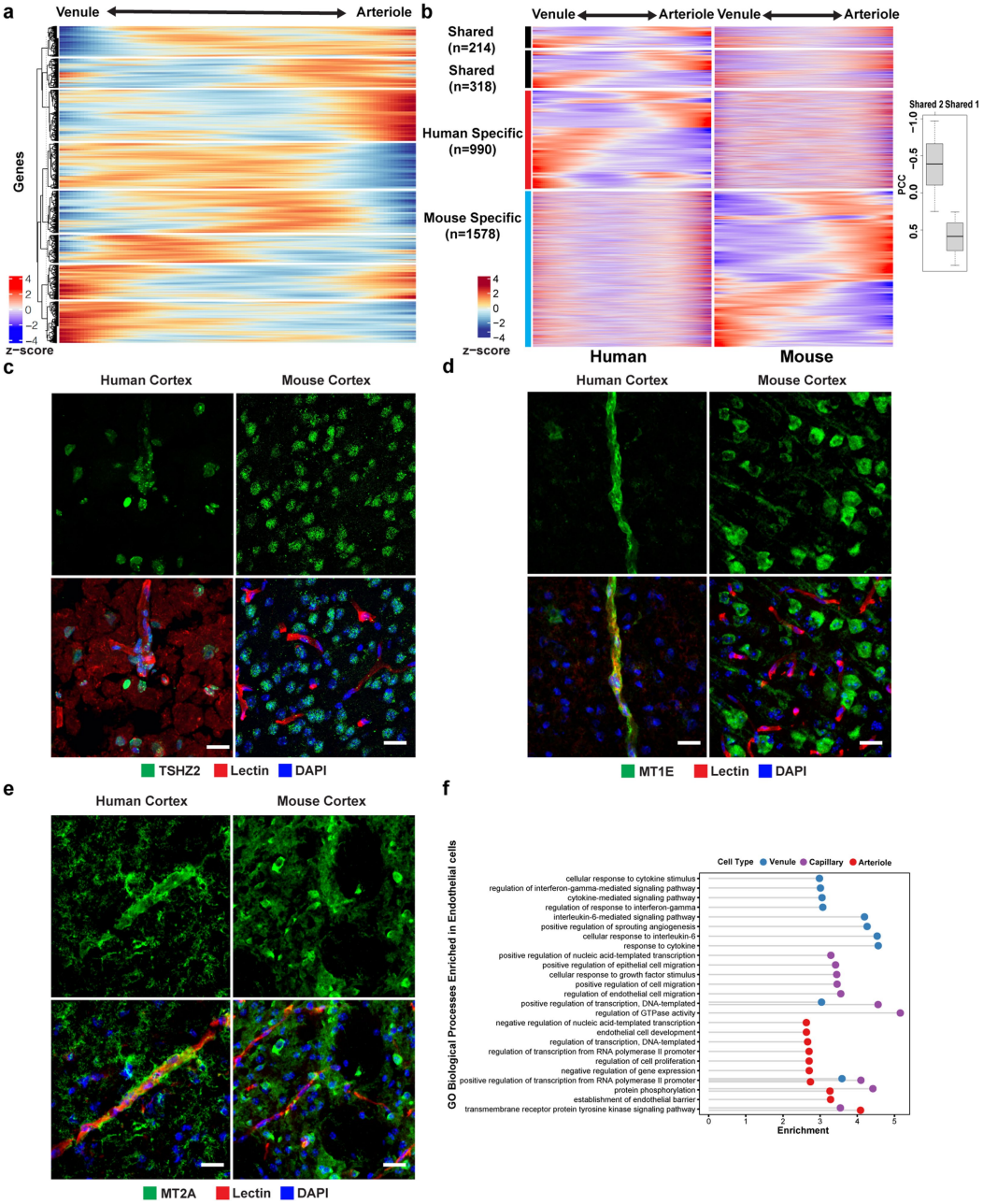

Extended Data Fig. 5 | Zonation in human brain endothelial cells. a. Gene zonation analysis of mouse brain endothelial cells from Vanlandewjick et al. **b**. Integrated zonation analysis of human and mouse brain endothelial cell profiles. Pearson correlation coefficient of shared genes shown on right. **c**. Indirect immunofluorescence of TSHZ2 expression in human and mouse brain cortex. **d**. Indirect immunofluorescence of MT1E/MT1 expression in human and mouse brain cortex. **e**. Indirect immunofluorescence of MT2A/MT2 expression in human and mouse brain cortex. **f**. Enriched Gene Ontology terms in endothelial zones. Representative images in **c.**, **d**., and **e**. from $n = 3$ independent biological replicates for each marker. Brightness and contrast enhanced for visualization. Scale bar, 20 µm.

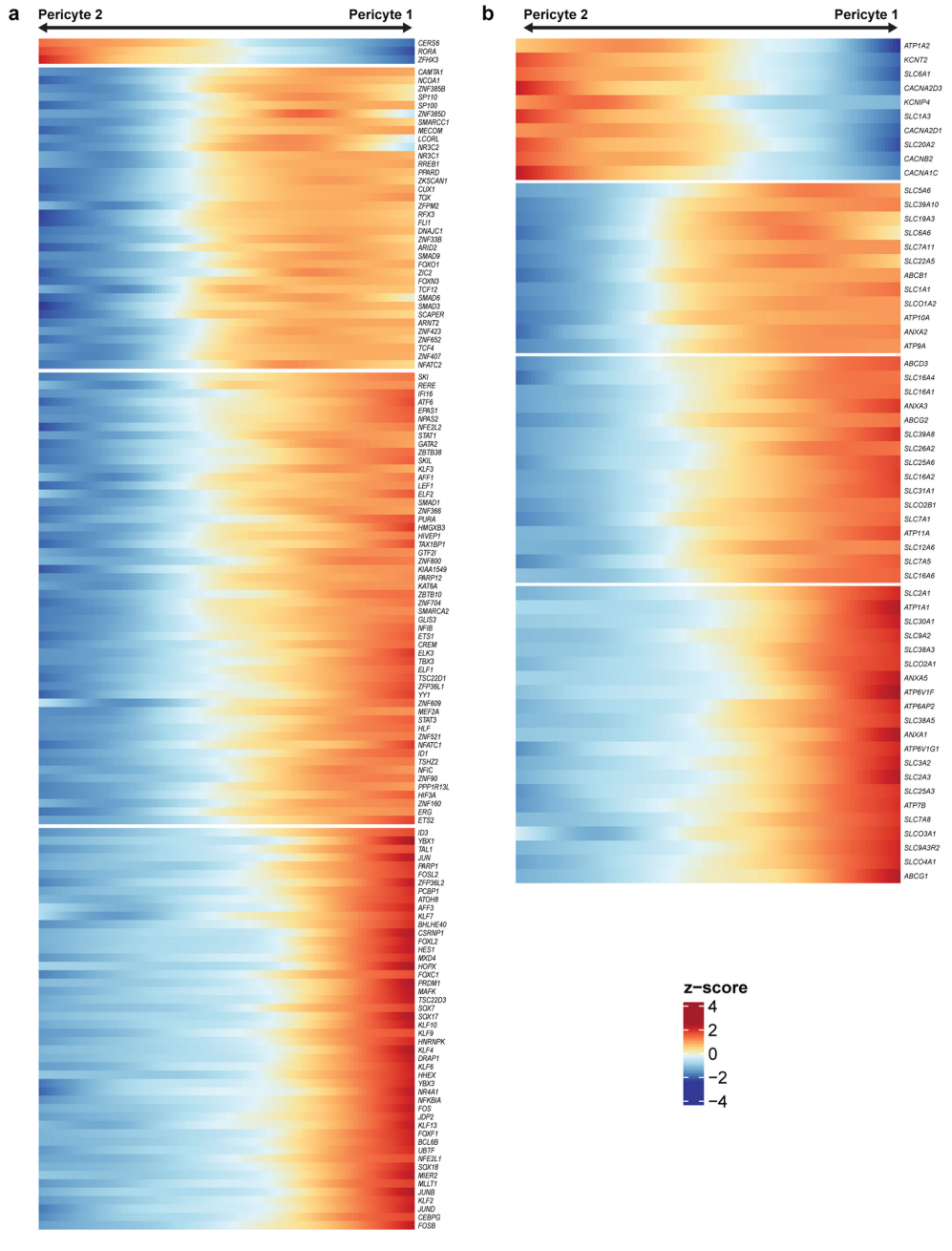

Extended Data Fig. 6 | Zonation gene expression analysis of human pericytes. a. Heatmap of zonated transcription factors along the pericyte gradient. **b**. Heatmap of zonated transporters along the pericyte gradient.

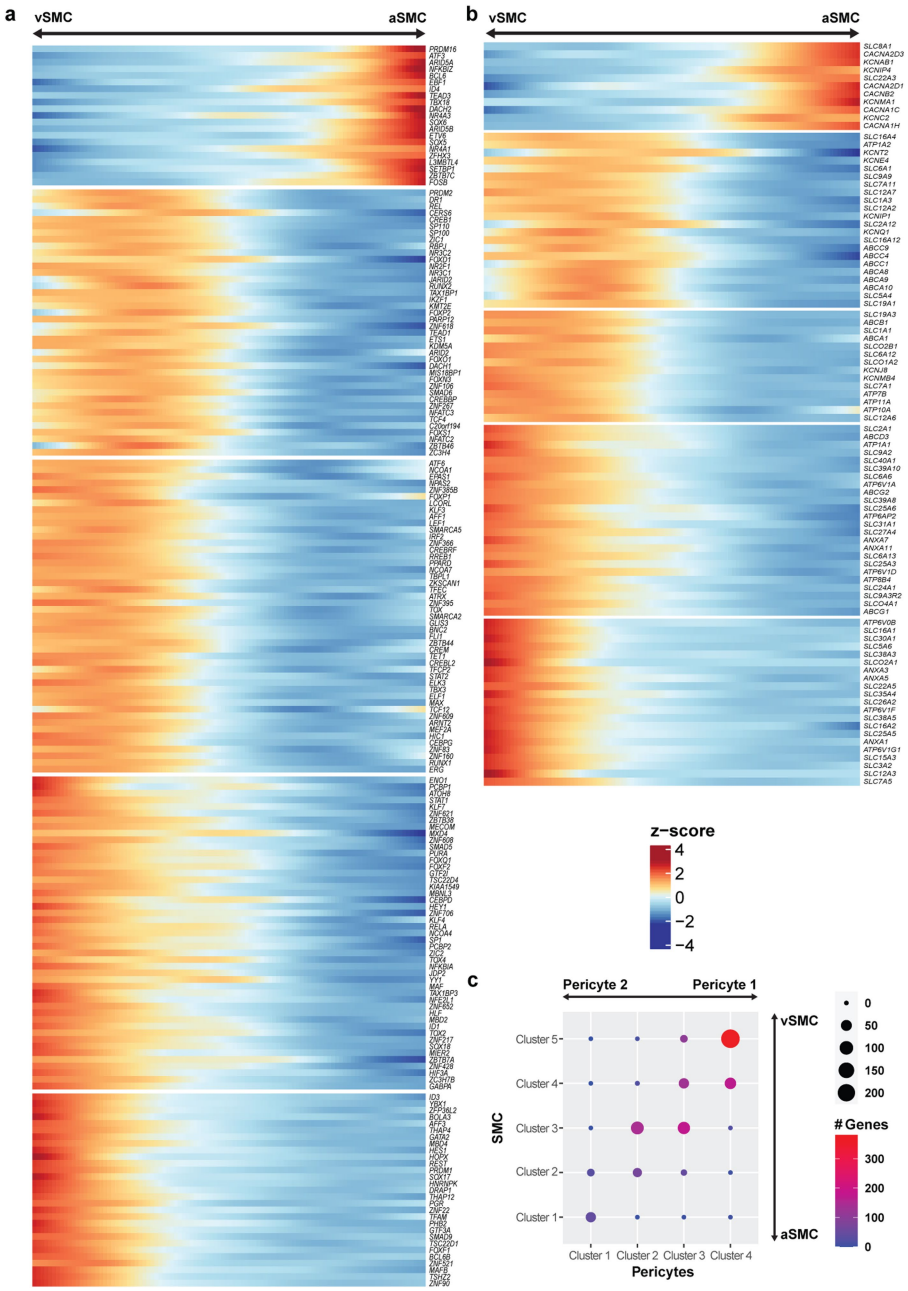

Extended Data Fig. 7 | Zonation gene expression analysis of human SMCs. a. Heatmap of zonated transcription factors along the SMC gradient. **b**. Heatmap of zonated transporters along the SMC gradient. **c**. Overlap matrix across the zonated pericyte and SMC clusters.

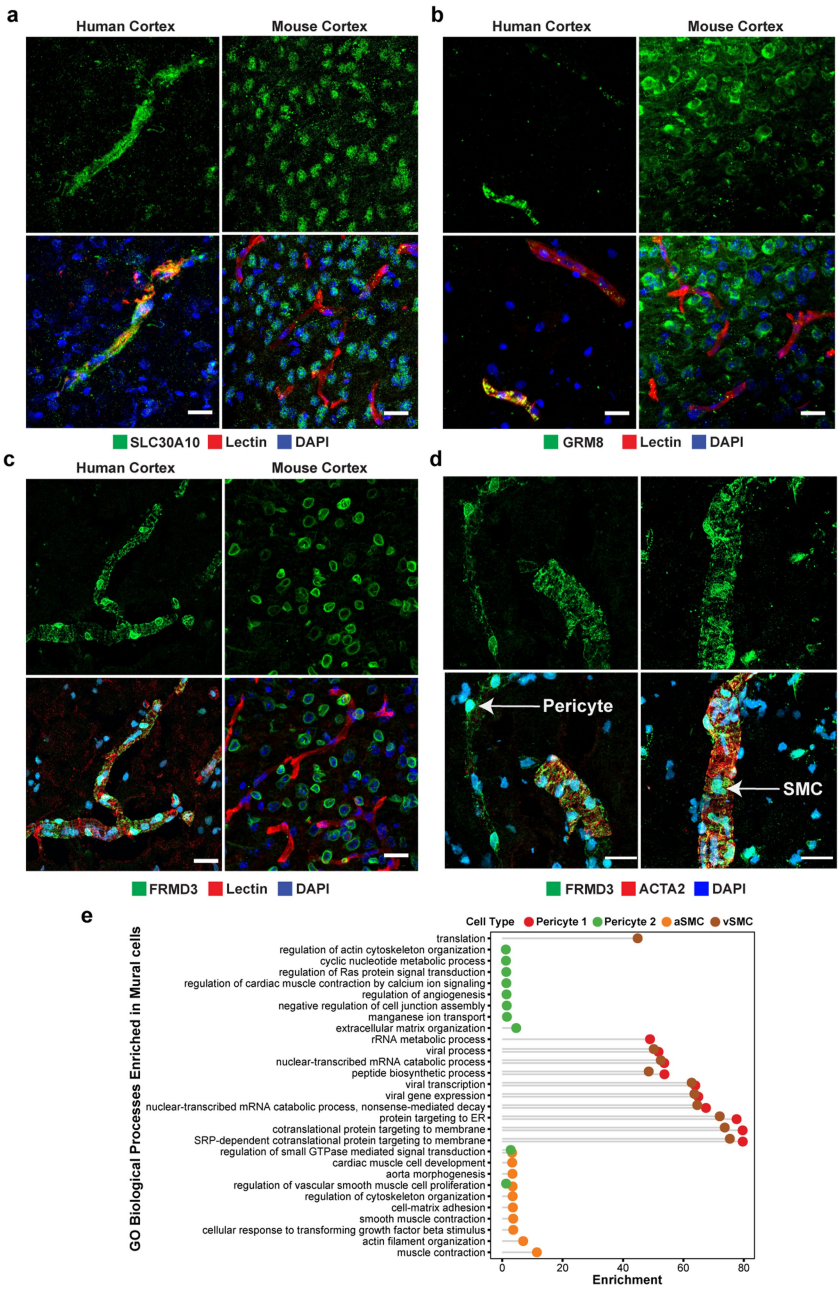

Extended Data Fig. 8 | Zonation in human brain mural cells. a. Indirect immunofluorescence of SLC30A10 expression in human and mouse brain cortex. **b**. Indirect immunofluorescence of GRM8 expression in human and mouse brain cortex. **c**. Indirect immunofluorescence of FRMD3 expression in human and mouse brain cortex. **d**. Indirect immunofluorescence localization of FRMD3 on ACTA2+ (known SMC marker) vessels. **e**. Enriched Gene Ontology terms in mural zones. Representative images in **a**–**d** from $n = 3$ independent biological replicates for each marker. Brightness and contrast enhanced for visualization. Scale bar, 20 µm.

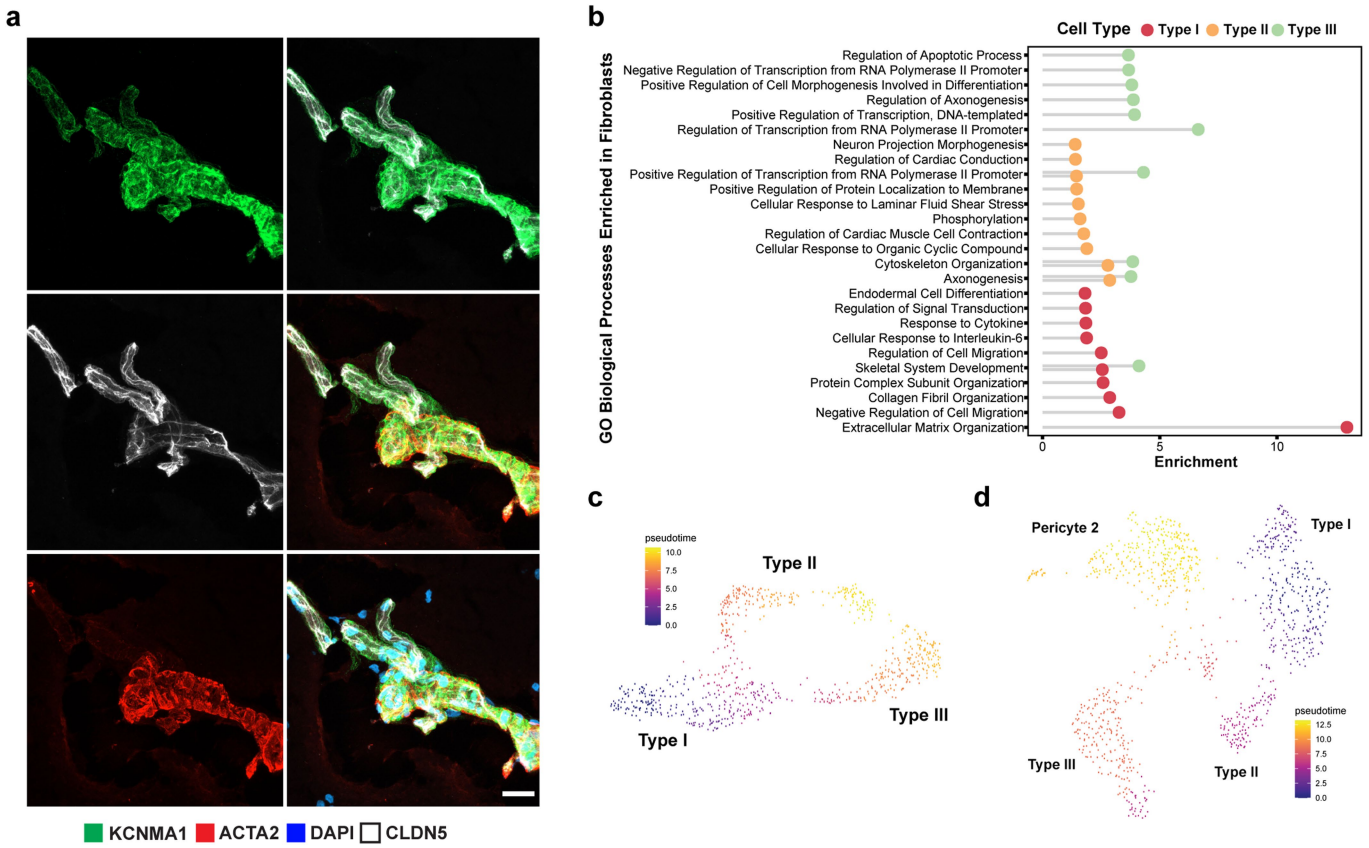

Extended Data Fig. 9 | Validation and pathway analyses of perivascular fibroblast subtypes. a. Immunofluorescence staining of Type III fibroblast marker KCNMA1 on ACTA2+ vessels in human. **b**. Enriched Gene Ontology analysis in perivascular fibroblast subtypes. **c**. Pseudotime analysis of *ex vivo* fibroblast subtypes. **d**. Pseudotime analysis of *ex vivo* fibroblast subtypes and Pericyte 2 (note: Pericyte 1 not shown as it did not fall within any pseudotime trajectory). Representative image in **a**. from n = 3 independent biological replicates for each marker. Brightness and contrast enhanced for visualization. Scale bar, 20 µm.

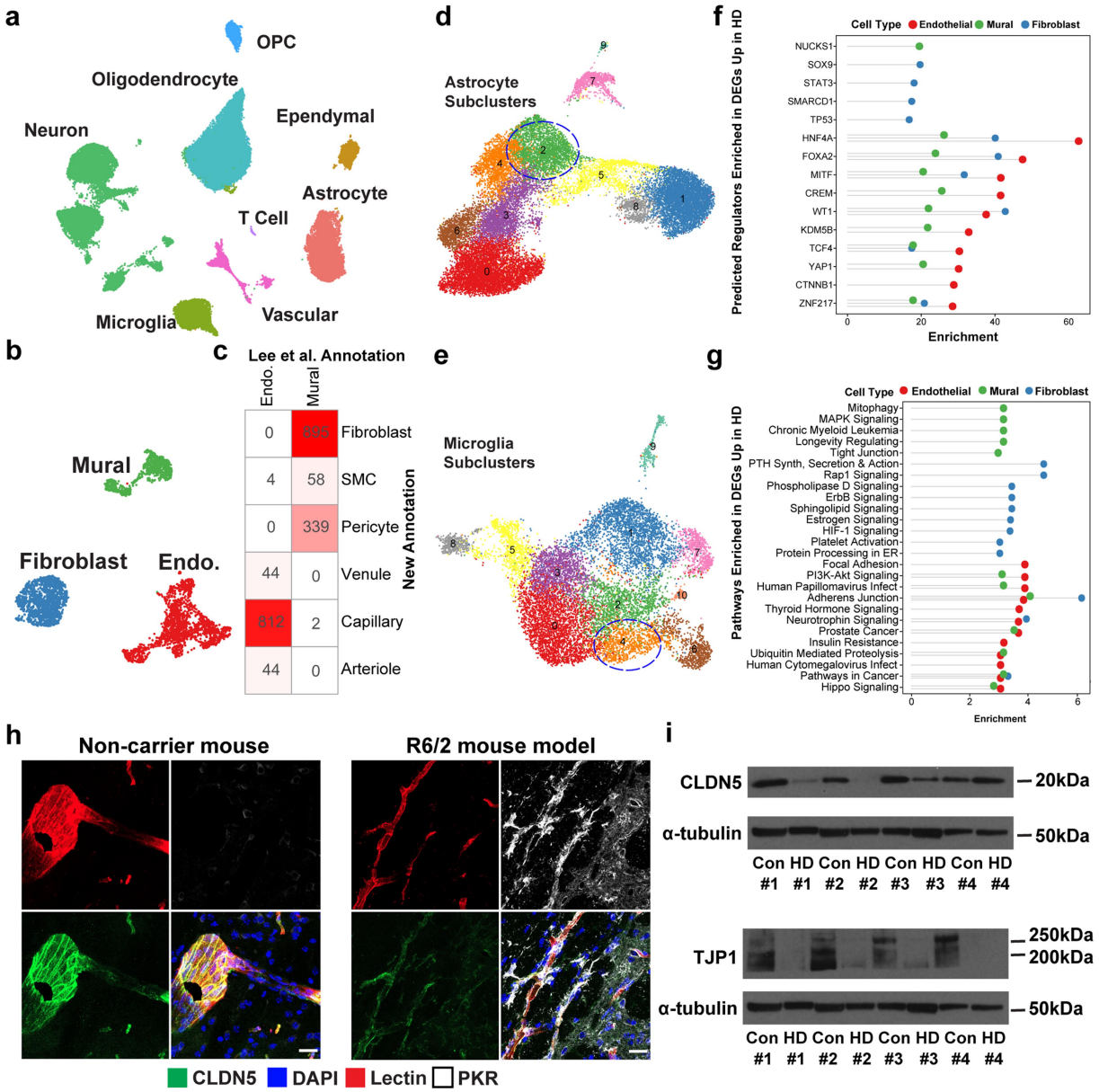

Extended Data Fig. 10 | Cerebrovascular profiling in Huntington's disease. **a**. UMAP of integrated single nuclei from *post mortem* control and HD human patient samples. **b**. UMAP of integrated cerebrovasculature cells in *post mortem* control and HD human patients. **c**. Comparison of cerebrovasculature cell annotations (in cell numbers) in this study vs. Lee et al. **d**. UMAP analysis of astrocyte subclusters in HD. Vascular-related astrocytes outlined in blue. **e**. UMAP analysis of microglia subclusters in HD. Vascular-related microglia outlined in blue. **f**. ChEA prediction of top 10 regulators of upregulated genes in HD endothelial, mural, and fibroblasts cells. **g**. Pathway analysis of the top 10 enriched upregulated pathways in HD endothelial, mural, and fibroblasts cells. **h**. PKR immunoreactivity in the R6/2 HD mouse model engulfs blood vessels with low CLDN5 expression. **i**. Western blots for tight junction proteins CLDN5 and TJP1 from human HD and control samples. Representative images in **h**. from $n = 3$ independent biological replicates for each immunostaining. Brightness and contrast in immunofluorescence enhanced for visualization. Scale bar, 20 µm.

nature research

Corresponding author(s): Myriam Heiman, Manolis Kellis

Last updated by author(s): Jan 25, 2022

Reporting Summary

Nature Research wishes to improve the reproducibility of the work that we publish. This form provides structure for consistency and transparency in reporting. For further information on Nature Research policies, see our Editorial Policies and the Editorial Policy Checklist.

Statistics

For all statistical analyses, confirm that the following items are present in the figure legend, table legend, main text, or Methods section.

n/a	Confirmed	
☐	☒	The exact sample size (*n*) for each experimental group/condition, given as a discrete number and unit of measurement
☐	☒	A statement on whether measurements were taken from distinct samples or whether the same sample was measured repeatedly
☐	☒	The statistical test(s) used AND whether they are one- or two-sided *Only common tests should be described solely by name; describe more complex techniques in the Methods section.*
☐	☒	A description of all covariates tested
☐	☒	A description of any assumptions or corrections, such as tests of normality and adjustment for multiple comparisons
☒	☐	A full description of the statistical parameters including central tendency (e.g. means) or other basic estimates (e.g. regression coefficient) AND variation (e.g. standard deviation) or associated estimates of uncertainty (e.g. confidence intervals)
☐	☒	For null hypothesis testing, the test statistic (e.g. *F*, *t*, *r*) with confidence intervals, effect sizes, degrees of freedom and *P* value noted *Give P values as exact values whenever suitable.*
☒	☐	For Bayesian analysis, information on the choice of priors and Markov chain Monte Carlo settings
☒	☐	For hierarchical and complex designs, identification of the appropriate level for tests and full reporting of outcomes
☒	☐	Estimates of effect sizes (e.g. Cohen's *d*, Pearson's *r*), indicating how they were calculated

Our web collection on statistics for biologists contains articles on many of the points above.

Software and code

Policy information about availability of computer code

Data collection	Sequencing data were collected with the Illumina NovaSeq6000 platform.
Data analysis	Cellranger v3.0.1, Seurat v3.2.0, DoubleFinder v2.0.3, MAST v1.16.0, Enrichr v3.0, ACTIONet v2.1.9, ImageJ; All code will be available at http://compbio.mit.edu/scBBB/ when the manuscript is accepted.

For manuscripts utilizing custom algorithms or software that are central to the research but not yet described in published literature, software must be made available to editors and reviewers. We strongly encourage code deposition in a community repository (e.g. GitHub). See the Nature Research guidelines for submitting code & software for further information.

Data

Policy information about availability of data

All manuscripts must include a data availability statement. This statement should provide the following information, where applicable:

- Accession codes, unique identifiers, or web links for publicly available datasets
- A list of figures that have associated raw data
- A description of any restrictions on data availability

Raw sequencing reads were aligned to the pre-mRNA annotated Mus musculus reference genome version GRCm38 or Homo sapiens reference genome version GRCh38. Code used in this study is available upon reasonable request from the corresponding authors. Count matrices for all cells analyzed in this study are uploaded with this submission as Supplementary Data and at http://compbio.mit.edu/scBBB/. Interactive website is available at https://nsun.shinyapps.io/scbbb/. Raw sequencing data associated with Figures 1-5 are publicly available in NCBI GEO under accession #GSE173731.

Field-specific reporting

Please select the one below that is the best fit for your research. If you are not sure, read the appropriate sections before making your selection.

☒ Life sciences ☐ Behavioural & social sciences ☐ Ecological, evolutionary & environmental sciences

For a reference copy of the document with all sections, see nature.com/documents/nr-reporting-summary-flat.pdf

Life sciences study design

All studies must disclose on these points even when the disclosure is negative.

Sample size	Sample-size calculation was not performed in this study. The number of patient samples used was estimated based on predicted number of cerebrovascular cells profiled per sample (approximately 300-500 cells per patient) to achieve a total of ~3,500 cerebrovascular cells (a benchmark set in previous work of Vanlandewijck, et al. 2018 https://doi.org/10.1038/nature25739). A total of 16 patient samples were used as described in Supplemental Table 1.
Data exclusions	All samples from patients with known genetic mutations were excluded from this study. Furthermore, given the nature of our study in understanding human cerebrovasculature we excluded all patients with known arteriovenous malformations. Finally, to avoid early developmental changes in transcriptional profiles, we restricted patient samples to be within age range of approximately 12-22 years of age. These details are also outlined in Methods section.
Replication	Various findings from the sequencing analyses were confirmed throughout the study at the protein level by indirect immunofluorescent staining using ex vivo tissue from three biologically independent samples. All attempts at replication were successful. Representative images shown in figures
Randomization	Randomization was not necessary in this study given the unbiased experimental approach. In analyzing snRNA-seq data, we projected each cell on a common two-dimensional embedding that corrects for covariates (age, sex, brain regions, sequencing platforms, post-mortem interval)
Blinding	Blinding was not necessary in this study given the unbiased experimental approach. In analyzing snRNA-seq data, cells cluster based on their transcriptional profiles, which does not require blinding given that cell type identities will cluster together regardless of condition

Reporting for specific materials, systems and methods

We require information from authors about some types of materials, experimental systems and methods used in many studies. Here, indicate whether each material, system or method listed is relevant to your study. If you are not sure if a list item applies to your research, read the appropriate section before selecting a response.

Materials & experimental systems

n/a	Involved in the study
☐	☒ Antibodies
☒	☐ Eukaryotic cell lines
☒	☐ Palaeontology and archaeology
☐	☒ Animals and other organisms
☒	☐ Human research participants
☒	☐ Clinical data
☒	☐ Dual use research of concern

Methods

n/a	Involved in the study
☒	☐ ChIP-seq
☒	☐ Flow cytometry
☒	☐ MRI-based neuroimaging

Antibodies

Antibodies used

Alexa-Fluor488 anti-Chicken, ThermoFisher, A11039, 1:500
Alexa-Fluor488 anti-Mouse, ThermoFisher, A21202, 1:500
Alexa-Fluor488 Plus anti-Rabbit, ThermoFisher, A32790, 1:500
Alexa-Fluor568 anti-Goat, ThermoFisher, A11057, 1:500
Alexa-Fluor546 anti-Rabbit, ThermoFisher, A10040, 1:500
Alexa-Fluor647 anti-Chicken, ThermoFisher, A21449, 1:500
Alexa-Fluor647 anti-Mouse, ThermoFisher, A32787, 1:500
Alexa-Fluor647 anti-Rabbit, ThermoFisher, A31573, 1:500
anti-TMEM16B, Abcam, ab113443, 1:100 dilution,
anti-CLDN5, ThermoFisher, 35-2500, 1:200 dilution, 1:1000 dilution (Western blot)
anti-TJP1, Abcam, ab216880, 1:1000 dilution (Western blot)
anti-FRMD3, Novus, NBP2-33879, 1:100 dilution
anti-CEMIP, LifeSpan Biosciences, LS-C108052-100, 1:100 dilution
anti-KCNMA1, LifeSpan Biosciences, LS-A9575-50, 1:100 dilution

anti-FBLN1, Millipore Sigma, HPA001612-100UL, 1:100 dilution
anti-metallothionein, Abcam, ab192385, 1:100 dilution
anti-VEGFC, Abcam, ab106512, reconstituted to 1 mg/ml in sterile PBS, 1:100 dilution
anti-MT1E, Abcam, ab193618, 1:100 dilution
anti-TSHZ2, LifeSpan Biosciences, LS-B9329-200, 1:100 dilution
anti-PKR, Abcam, ab32052, 1:200 dilution
anti-TRPM3, Abcam, ab56171, 1:100 dilution
anti-GRM8, Lifespan Biosciences, LS-A922-50, 1:100 dilution
anti-SLC20A2, Lifespan Biosciences, LS-C334915, 1:100 dilution
anti-SLC30A10, Abcam, ab229954, 1:300 dilution
anti-GFAP, Abcam, ab4674, 1:400 dilution
anti-AQP4, Millipore Sigma, AB2218, 1:100 dilution
anti-ACTA2, Lifespan Biosciences, LS-B3933, 1:100 dilution
Lycopersicon Esculentum (Tomato) Lectin (LEL, TL), DyLight® 488, Vector Laboratories, DL-1174-1, 1:200 dilution
Lycopersicon Esculentum (Tomato) Lectin (LEL, TL), DyLight® 594, Vector Laboratories, DL-1177-1, 1:200 dilution
Lycopersicon Esculentum (Tomato) Lectin (LEL, TL), DyLight® 649, Vector Laboratories, DL-1178-1, 1:200 dilution
Goat anti-Mouse IgG HRP, ThermoFisher, 31430, 1:10,000 dilution
Goat anti-Rabbit IgG HRP, ThermoFisher, 31460, 1:10,000 dilution

Validation

All primary antibodies were used for indirect immunofluorescence experiments as validation for single nuclear RNA sequencing data analysis. All antibodies used have confirmed reactivity with human targets or human/mouse targets whenever used in cross-species comparisons. To confirm primary staining, we validated antibody signal in three ways: 1) negative controls using only secondary antibodies, 2) expression in expected cell type as predicted by transcriptomic analysis, and 3) in the case of co-staining, imaging at channels with minimal spectral overlap (i.e. 488nm and 647nm). For all antibodies, additional information on key publications and immunogen (if available) can be found on manufacturer's website.

Animals and other organisms

Policy information about studies involving animals; ARRIVE guidelines recommended for reporting animal research

Laboratory animals	All animal experiments were approved by the MIT Committee on Animal Care. Mice were grouped housed with food and water provided ab libitum on a standard 12h light/12h dark cycle. 6-week old male C57BL/6J wild-type mice (Jackson Laboratories stock #000664) were used for snRNA-seq and immunofluorescence experiments. 9-week old male B6CBA-Tg(HDexon1)62Gpb/1J mice (CAG repeat length 160 ± 5; Jackson Laboratories stock # 002810) and non-carrier controls were used for R6/2 experiments. No prior procedures were performed on any animal prior to experiments.
Wild animals	No wild animals were used in this study.
Field-collected samples	No field-collected samples were used in this study.
Ethics oversight	MIT Committee on Animal Care

Note that full information on the approval of the study protocol must also be provided in the manuscript.